Journal of Neuroinflammation

RESEARCH

Open Access

Sex chromosomes and sex hormones differently shape microglial properties during normal physiological conditions in the adult mouse hippocampus

Bianca Caroline Bobotis[1,2], Mohammadparsa Khakpour[1,2], Olivia Braniff[1,2], Elisa Gonçalves de Andrade[1], Makenna Gargus[1,2], Micah Allen[1,2], Micaël Carrier[1,3,4], Joanie Baillargeon[3], Manu Rangachari[3,5] and Marie-Ève Tremblay[1,2,3,5,6,7,8*]

Abstract

The brain presents various structural and functional sex differences, for which multiple factors are attributed: genetic, epigenetic, metabolic, and hormonal. While biological sex is determined by both sex chromosomes and sex hormones, little is known about how these two factors interact to establish this dimorphism. Sex differences in the brain also affect its resident immune cells, microglia, which actively survey the brain parenchyma and interact with sex hormones throughout life. However, microglial differences in density and distribution, morphology and ultrastructural patterns in physiological conditions during adulthood are largely unknown. Here, we investigated these aforementioned properties of microglia using the Four Core Genotypes (FCG) model, which allows for an independent assessment of gonadal hormones and sex chromosomal effects in four conditions: FCG XX and Tg XY^{-} (both ovaries); Tg XX^{Sry} and Tg XY^{Sry} (both testes). We also compared the FCG results with XX and XY wild-type (WT) mice. In adult mice, we focused our investigation on the ventral hippocampus across different layers: CA1 *stratum radiatum* (Rad) and CA1 *stratum lacunosum-moleculare* (LMol), as well as the dentate gyrus polymorphic layer (PoDG). Double immunostaining for Iba1 and TMEM119 revealed that microglial density is influenced by both sex chromosomes and sex hormones. We show in the Rad and LMol that microglia are denser in FCG XX compared to Tg XY^{Sry} mice, however, microglia were densest in WT XX mice. In the PoDG, ovarian animals had increased microglial density compared to testes animals. Additionally, microglial morphology was modulated by a complex interaction between hormones and chromosomes, affecting both their cellular soma and arborization across the hippocampal layers. Moreover, ultrastructural analysis showed that microglia in WT animals make overall more contacts with pre- and post-synaptic elements than in FCG animals. Lastly, microglial markers of cellular stress, including mitochondrion elongation, and dilation of the endoplasmic reticulum and Golgi apparatus, were mostly chromosomally driven. Overall, we characterized different aspects of microglial properties during normal

*Correspondence:
Marie-Ève Tremblay
evetremblay@uvic.ca

Full list of author information is available at the end of the article

physiological conditions that were found to be shaped by sex chromosomes and sex hormones, shading more light onto how sex differences affect the brain immunity at steady-state.

Keywords Microglia, Sex differences, Mouse, Four core genotypes, Density, Distribution, Morphology, Ultrastructure, Hippocampus, Scanning Electron Microscopy

Introduction

The brain exhibits clear structural and functional differences based on sex [1–3]. It is widely acknowledged that various factors, such as genetics, epigenetics, and hormonal influences, contribute to these sex differences [4]. In addition, a large number of central nervous system (CNS)-related diseases exhibit sexual dimorphism. However, little is known about the factors that shape these differences and how to address them in developing novel treatments [5–7].

Biological sex is determined by sex chromosomes and sex hormones [8, 9]. This process is led by genes located on the sex chromosomes and the release of sex hormones, especially androgens and estrogens, coming primarily from the gonads and exerting effects on the body, brain, and behavior [10–13]. Sex differences also extend to individual cells within the brain parenchyma, including microglia [3, 14, 15].

Microglia, which are the resident innate immune cells of the CNS, are highly affected by sex hormones [14, 16–20]. These cells are essential for brain development and play a crucial role in preserving the health of the CNS, maintaining its homeostatic balance when challenged by infectious or inflammatory cues [21, 22]. Microglia promote and assist with various processes within the CNS, closely interacting with neurons, other glial cells, the neurovascular unit and the extracellular matrix. These cells not only regulate axonal myelination, but also contribute to synaptic pruning, vasculature repair, and clearance of debris and toxic substances, among other important physiological roles [23–28].

Originating from the embryonic yolk sac, microglia migrate and colonize the brain during early development, around embryonic day (E)9.5 in mice. This precedes a hormonal surge in the brain, with androgens and estrogens peaking at around E17.5–18 [29–34]. Notably, microglia can express receptors for ovarian hormones such as estradiol, and for testicular hormones like testosterone [35–37]. Dysregulation of microglial functions is associated with several health concerns that often show sex prevalences, not only affecting Alzheimer's disease, which shows more prevalence among females, and Parkinson's disease, more male-prevalent, but also including various other neurodevelopmental, neuropsychiatric and neurodegenerative disorders [38–43]. As microglia are important immune sentinels during life, it is important to study sex differences in their properties during normal physiological conditions to provide insights into their possible alterations in disease.

During normal physiological conditions, it has been shown that adult male mice tend to exhibit denser microglia in the hippocampus, cortex, and amygdala, whereas female rats typically display longer and more extensively branched microglial processes in the prefrontal cortex around adolescence, indicating possible differences in microglial surveillance between sexes, brain regions and time points [44–46]. Additionally, gene expression of microglia differs between males and females [44, 45]. In adult mice, bulk-RNA sequencing from the hippocampus of purified Cd11b-positive ($^{+}$) microglia showed that males had higher levels of genes associated with regulation of the defense response to bacteria, insulin receptor pathway, glial differentiation, and ATP binding. In contrast, females had higher differently expressed genes that were associated with GABA and glutamate receptor activity, ubiquitin protein activity, and magnesium ion transport [44]. Nevertheless, the precise mechanisms underlying these differences in microglial density and morphology between sexes remain unclear, particularly the influence of sex hormones and chromosomal factors, and whether there is a singular determinant or a combination of factors driving these differences. Overall, limited research has been conducted examining microglial sex differences during normal physiological conditions, specifically addressing possible variations in their density, distribution, morphology, and ultrastructure across sexes during adulthood. This evaluation could aid the establishment of a baseline, in terms of various microglial properties (e.g., density, distribution, morphology, ultrastructure), which can become altered in disease or with exposure to various challenges (e.g., stress, diet, infection) across life.

To investigate closely the roles of sex chromosomes and gonadal hormones in driving differences in microglial properties between sexes during normal physiological conditions, we used the Four Core Genotypes (FCG) mouse model, which allows for an independent assessment of gonadal hormones and sex chromosomal effects [47–49]. While the sex determining region Y (*Sry*) gene is required for male testes formation, in this mouse model, this gene is excised from the Y chromosome and inserted into an autosome, creating four sex chromosome-gonad combinations: XX with ovaries (FCG XX), XY with ovaries (Transgenic (Tg) XY^{-}), XX with testes (Tg XX^{Sry}), or XY with testes (Tg XY^{Sry}) [48]. As microglia are highly

affected by hormonal and transcriptional changes, female and male wild-type mice (WT XX and WT XY) were also used for validation [10, 13, 18, 44, 50].

We focused our investigation on different hippocampal strata: cornu ammonis (CA)1 *stratum radiatum* (Rad) and CA1 *stratum lacunosum-moleculare* (LMol), as well as the dentate gyrus polymorphic layer (PoDG), which are some of the well-established sexually dimorphic regions, in which microglia display sex-specific differences in various properties [51–53]. The hippocampus is an important brain region involved in the consolidation and storage of long-term memories, cognition and emotional processing [54, 55]. This area is also rich in estradiol receptors where neurons locally synthesize estrogen and testosterone during adulthood, particularly the pyramidal neurons of the CA1 and the granule cells of the DG [51–53]. Few other studies have shown sex-specific differences in microglia between regions and layers of the hippocampus [16, 56–58], with previous research typically examining the CA1 and/or DG as a whole considering their roles in learning and memory [44, 59] or looking at other brain regions important for emotional/fear processing and sexual behavior, such as the amygdala or the preoptic area (POA) [18, 60, 61].

Hence, we hypothesized that both sex hormones and sex chromosomes would play a major role in modifying microglial density, distribution, morphology and ultrastructure during physiological conditions. We aimed to deliver thorough qualitative analyses of microglial properties in the FCG model, using WT as a baseline to validate the model's robustness and reliability, and provide useful information for future studies across other conditions.

By analysing the ventral hippocampus CA1 Rad, CA1 LMol and the PoDG, we demonstrate, in adult mice, that microglial density, distribution and morphology are strongly influenced by both sex hormones and chromosomes. In the Rad and LMol we observed an interaction between sex hormones and chromosomes, whereas in the PoDG, the effects were predominantly driven by sex hormones. Additionally, we found that microglial ultrastructure – particularly markers of cellular stress, such as mitochondrial elongation and dystrophy, endoplasmic reticulum (ER) and Golgi apparatus dilation, and extracellular digestion – was primarily influenced by chromosomal factors.

Methods

Animals

All studies and procedures were approved by the Université Laval (2021-830 and 2023-1372) and the University of Victoria (AUP 2020-013) animal care committees, strictly following the recommendations from the Canadian Council on Animal Care.

The FCG mice were generated at Université Laval using B6.Cg-Tg(Sry)2Ei ^{Srydl1Rlb}/ArnoJ mice purchased from The Jackson Laboratory (Stock#010905; RRID:IMSR_Jax:010905). The FCG mice harbor two mutations. The first one is Y^- (dl1Rlb allele), an 11 kb deletion of the testes determining region gene (*Sry*) on the Y chromosome [48]. Mice carrying the Y^- allele possess a Y chromosome, however, as the *Sry* was deleted, they undergo development as gonadal females, exhibiting ovaries rather than testes [62]. The second mutation involves the insertion of the Tg(Sry)2Ei transgene (a clone of the deleted *Sry*), onto an autosome – specifically on chromosome 3, wherein this sequence does not disrupt any identified genes [47]. The combined mutations transfer the testes determination from the Y chromosome to an autosome, so that the determination of testes development occurs independently from the complement of X or Y chromosomes [48, 63]. Breeding these mice with WT C57BL/6J XX females produce the FCG. In this study, we utilized: FCG XX females that possess neither mutant allele and develop ovaries (but were generated through the breeding of the Tg(Sry)2Ei transgene); Tg XY^{Sry} – chromosomally and hormonally male mice expressing the *Sry* allele; Tg XX^{Sry} – originally XX mice but expressing the *Sry* allele, thus developing as gonadal males with testes; Tg XY^- – originally XY mice, but lacking the *Sry* gene, thus developing ovaries; lastly, as a control, we used C57BL/6J female and male WT mice (WT XX and WT XY). Mice at the Université Laval and at the University of Victoria were housed under a 12-hour light – dark cycle with both light onsets at 7 a.m. and *ad libitum* access to food and water.

Intracardiac perfusion and fixation

For each genotype, four to five adult mice – obtained from three different litters and five generations of breeding – at postnatal day (P)110 were anesthetized with a mix of ketamine (100 mg/kg)/xylazine (10 mg/kg) and intracardially perfused – infusion pump speed of 24 mL/min for 10 min. The blood was flushed using ice-cold phosphate-buffered saline (PBS; 50 mM, pH 7.4), followed by 4% paraformaldehyde/0.6% glutaraldehyde between 8 a.m. and 10 a.m. After skull removal, brains were post-fixed with 4% paraformaldehyde for 2 h at 4 °C, and subsequently, PBS washes were performed. Coronal brain sections at a 50-µm thickness were cut in ice-cold PBS using a vibratome (VT1200S, Leica Biosystems) and stored at -20 °C in cryoprotectant (30% (v/v) glycerol and 30% (v/v) ethylene glycol in PBS) until further processing.

Immunofluorescent staining and imaging

Immunofluorescence staining against ionized calcium-binding adapter molecule 1 (Iba1) and transmembrane protein 119 (TMEM119), common markers for microglial

visualization, was performed as previously described [64]. While Iba1, a cytoplasmatic protein responsible for cytoskeletal reorganization, is also expressed by peripheral macrophages; TMEM119 is an important regulator of the Wnt/β-catenin pathway, being, so far, selectively expressed by yolk sac-derived cells in the adult CNS during normal physiological conditions [65–67].

Sections containing the ventral portion of the hippocampus (VH; Bregma – 2.79 mm to -3.63 mm) were selected based on the stereotaxic atlas of Paxinos and Franklin [68]. For each condition, five brain sections from each of four or five mice per group were processed. For fluorescent microscopy, sections were washed with fresh PBS and quenched with sodium citrate buffer (10 mM with 0.5% Tween 80, pH 6.0) at 70 °C. After cooling down, sections were washed with PBS and incubated with freshly made 1% $NaBH_4$ for 30 min. After PBS washing, the sections were incubated with 0.3% H_2O_2 for 30 min. A blocking solution containing 10% normal donkey serum, 0.5% fish gelatin and 0.01% Triton X-100 was applied to the sections for 60 min at room temperature (RT). Sections were then incubated with a cocktail of primary antibodies: mouse anti-Iba1 antibody (1:150 in blocking buffer, cat# MABN92, Sigma-Aldrich) and rabbit anti-TMEM119 (1:300, in blocking buffer, cat# ab209064, Abcam) at 4 °C overnight. After the overnight incubation period, the sections were rinsed with 0.01% Triton X-100 in PBS (PBS[T]) before incubating with a cocktail of secondary fluorescent antibodies: donkey anti-mouse Alexa Fluor® 555-conjugated (1:300 in blocking buffer, cat# A-31570, Invitrogen) and donkey anti-rabbit Alexa Fluor® 647-conjugated (1:300 in blocking buffer, cat# A-31573, Invitrogen) for 90 min at RT. Finally, after PBS[T] rinse, sections were counter-stained with DAPI (4′,6-diamidino-2-phenylindole; 1:20000, Thermo-scientific) and mounted onto glass slides, followed by coverslipping with Fluoromount-G, an anti-fading mounting medium (cat# 00-4958-02, Invitrogen).

Immunofluorescent images of the VH CA1 Rad and LMol and of the PoDG were acquired from all the processed sections. For microglial cellular density and distribution analysis, imaging at 20× was performed with an Axio Imager M2 epifluorescence microscope equipped with an AxioCamMR3 camera (Zeiss, Oberkochen, Germany). For microglial morphology analysis, a Zeiss LSM-880 confocal microscope (Zeiss, Oberkochen, Germany) was used to acquire z-stacks with a 63× objective (numerical aperture of 1.4) in Airyscan mode. An interval of 0.19 µm was used between images within each stack (~ 50 slices), while focus stacking was performed using the Zen 3.1 software (Blue edition, Zeiss).

Immunoperoxidase staining and electron microscopy

For scanning electron microscopy (SEM) imaging and ultrastructural analyses, brain sections were immunostained against Iba1. Sections containing the VH (Bregma – 2.79 mm to -3.63 mm) were selected based on the stereotaxic atlas of Paxinos and Franklin [68]. For each condition, two to three brain sections from each of four mice per group were processed. First, the sections were washed with fresh PBS and quenched with 0.3% H_2O_2 for 5 min at RT. After a quick wash with PBS, the sections were incubated with $NaBH_4$ 0.1% for 30 min to reduce aldehydes from the perfusion. The sections were next immersed in a blocking solution containing 10% fetal bovine serum, 3% bovine serum albumin and 0.01% Triton X-100 in Tris-buffered saline (TBS: 0.05 M, pH 8.0) for 60 min at RT. Shortly after, they were incubated in primary antibody, rabbit anti-Iba1 (1:1000 in blocking buffer, cat# 019-19741, FUJIFILM Wako Chemical) at 4 °C overnight. The following day, after acclimating, the antibody was washed out followed by the goat anti-rabbit secondary biotinylated polyclonal antibody incubation (1:300, in TBS, cat# 111-066-046, Jackson ImmunoResearch) at RT for 2 h. Lastly, the sections were incubated with avidin-biotin complex solution (1:1000 in TBS; cat# PK-6100, Vector Laboratories) for 60 min at RT. Staining was revealed in Tris buffer (TB: 0.05 M, pH 8.0) containing 0.05% diaminobenzidine (DAB; cat# D5905-50TAB, Merck KGaA Darmstadt) and 0.015% hydrogen peroxide. Following the immunostaining, the sections were incubated in osmium-thiocarbohydrazide-osmium. They underwent a sequential treatment: incubation in a mixture of 3% ferrocyanide (cat# PFC232.250, BioShop) diluted in double-distilled water (1:1) with 4% aqueous osmium tetroxide (cat#19170, Electron Microscopy Sciences) for 60 min, followed by immersion in 1% thiocarbohydrazide diluted in double-distilled water (cat# 2231-57-4, Electron Microscopy Sciences) for 20 min, and then in 2% osmium tetroxide diluted in double-distilled water for 30 min. Subsequently, they underwent dehydration in progressively increasing concentrations of ethanol (35 – 100%), followed by three 5-minute propylene oxide washes. Following post-fixation, brain sections were immersed overnight in Durcupan ACM resin (cat# 44611–44614, Merck KGaA Darmstadt). The next day, these sections were sandwiched between two fluoropolymer sheets (ACLAR®; cat# 50425-25, Electron Microscopy Sciences), coated with a thin layer of resin, and left to polymerize at 55 °C for 72 h. The region of interest (ROI), only CA1 Rad, located in the VH, were excised from the flat-embedded sections on ACLAR® sheets and affixed to the tops of resin blocks. Ultrathin sections (~ 75 nm) were then produced using an ultramicrotome (Ultracut UC7 ultramicrotome, Leica Biosystems), collected on a silicon nitride chip, and attached to specimen

mounts for SEM. A Crossbeam 540 field emission SEM with a Gemini column (Zeiss) was operated at a 1.4 kV voltage and 1.2 nA current. Finally, we randomly imaged at 5 nm of resolution a total of 10 to 12 microglial cell bodies (Iba1$^+$ or negative ($^-$)) per animal.

Density and morphology analyses

The images were blinded to the experimental groups and analysed using Fiji (NIH; v.1.53), as previously reported [56, 64]. For this analysis, five sections from each of five mice per group were used. The CA1 Rad, CA1 LMol and PoDG regions were initially outlined utilizing the Freehand selection tool, with reference to the Paxinos and Franklin stereotaxic atlas [68]. Subsequently, the area of the ROI was measured in pixels followed by its conversion into mm^2. The evaluation of microglial density and distribution was carried out on all the processed and imaged sections. In this analysis, Iba1$^+$/TMEM119$^+$ cells were identified as microglia, and the counts of microglial cells were performed manually. The microglial density value was determined as the total number of cells divided by the total area (in cells/mm^2). The distribution of Iba1$^+$/TMEM119$^+$ cells was determined by measuring the average distance of each positive cell to its closest neighbor. In particular, the nearest neighbor distance was obtained using the Nearest Neighbor Distance Plugin developed by Yuxiong Mao. Typically, the nearest neighbor distance is inversely correlated with density, making it a complementary measure to both density and the spacing index. Moreover, the spacing Index (measured in arbitrary units, a.u.) was determined by multiplying microglial density (cells/mm^2) by the square average of the nearest neighbor distance for each ROI, and it reflects how evenly spaced the cells are, further complementing the density analysis. The same density and distribution analysis protocol was performed for the Iba1$^+$/TMEM119$^-$ cells (identified as peripheral myeloid infiltrating macrophages/monocytes) and Iba1$^+$/TMEM119$^{+/-}$ cells (total microglia and infiltrating macrophages/monocytes) [64, 69].

For the microglial morphology analyses, 15 Iba1$^+$/TMEM119$^+$ cells/animal/condition were randomly imaged across at least three different brain sections per animal in each of the CA1 Rad, CA1 LMol and PoDG (totalizing 1,350 analysed cells). Imaging of the brain regions was performed with reference to the Paxinos and Franklin stereotaxic atlas [68] and subsequently blinded to the experimental groups before analyses. Manually, each cell soma and arborization were traced using the Freehand and Polygon tools in Fiji. Area (in μm^2) and perimeter (in μm) as well as shape descriptors (e.g., circularity and solidity, in a.u.) were obtained. Specifically, the arbor circularity was calculated through $4\pi \times (\text{area}/\text{perimeter}^2)$, where a value of 1.0 represents a perfect circle and a value of 0.0 corresponds to an elongated shape. Solidity was obtained by dividing the cell area by the convex cell area, with a value of 0.0 indicating a porous/rugous shape and 1.0 a convex shape [16]. These parameters have been widely utilized and illustrated in previous research [70]. Our final sample size for both density and morphology analysis are reported in averaged values per animal/group.

Ultrastructural analyses

The microglial ultrastructural analyses was performed using QuPath (v.0.4.4) [71] on images blinded to both animal and group, following an adaptation from our previous work [56, 64]. For this analysis, two to three brain sections from each of four mice per group were used. In total, we analysed 271 microglia, with 10 to 12 cells per animal/group. Identification of microglial cell bodies relied on positive staining for Iba1 and/or their unique heterochromatin pattern and distinctive ultrastructural features, including smaller cell bodies and nuclei compared to adjacent astrocytes and neurons, long stretches of ER, and, the presence of diverse inclusions (e.g., lysosomes) dispersed heterogeneously in their cytoplasm [72]. Quantification involved assessing microglial contacts with other cell types (astrocytes and neuronal cell bodies), myelinated axons, blood vessels, and synaptic elements (pre-synaptic axon terminals and post-synaptic dendritic spines).

Neuronal cell bodies were distinguished by their pale cytoplasm and nuclei, with the presence of one or more electron-dense nucleoli as well as small patches of heterochromatin. They frequently made direct contacts with pre-synaptic axon terminals. Astrocytic cell bodies were identified by their pale nuclei with a thin rim of heterochromatin and pale irregular cytoplasm [16, 28, 73]. Pre-synaptic axon terminals were identified by their synaptic vesicles (with a minimum of five vesicles for recognition), while post-synaptic dendritic spines were in direct contact with a pre-synaptic axon terminal and displayed a visible post-synaptic density. Myelinated axons were identified by their electron-dense sheaths and granular cytoplasm, while extracellular space pockets were characterized by clear spaces around microglial cell bodies and/or processes without delineating membranes. Microglia are known to interact with dendrites and perineuronal nets in the brain parenchyma, playing a role in synaptic modulation and extracellular matrix remodeling [23, 65]. These cells can also release lysosomal enzymes to degrade extracellular components, a process known as digestive exophagy [74, 75]. Hence, extracellular digestion was identified by extracellular pockets containing debris directly adjacent to a microglial cell body [16, 28, 73].

In microglial cell bodies, the health status or functional state of the ER/Golgi apparatus, lysosomes,

mitochondria, and phagosomes were assessed. Criteria included the identification of ER/Golgi dilation (when the cisternae had an electron-lucent appearance and the intracisternal distance was 100 nm or more), elongated mitochondria (when the length was above 1000 nm) and dystrophic mitochondria (swollen mitochondria with abnormal cristae structure or vacuoles) [28, 38, 76]. Additionally, we identified primary, secondary and tertiary lysosomes [28, 57]. Primary lysosomes were recognized by their small size, with a round shape and single-membrane enclosure, dense and uniform "salt and pepper" texture. Secondary lysosomes were distinguished by their frequent endosomes, the presence of small lipid droplets, and uneven texture. Tertiary lysosomes were identified by their bigger size and association with lipofuscin granules and lipid droplets [28, 57]. Immature lysosomes comprised both primary and secondary lysosomes. Phagosomes were identified by their single-membrane enclosure and discriminated between empty and with content states. The presence of content was defined as electron-dense material contained in the phagosome. Autophagosomes were identified by their double-membrane enclosure [28, 27, 57].

To analyse the nuclear and cytoplasmic area, perimeter, and shape of the microglial cell body, the outline of each microglial cytoplasmic and nuclear membrane was traced using the Freehand selection tool in ImageJ. Subsequently, shape descriptors (area, perimeter, solidity, and circularity) were evaluated [77, 78].

The ultrastructure analysis involved absolute (e.g., the number of a specific feature per microglial cell body) and relative values (e.g., the percentage of microglial cell bodies presenting a particular feature). Our final sample size is reported in absolute values per cell/group.

Statistical analyses

Statistical analyses were performed on GraphPad Prism software (Massachusetts, USA; v.10.3.1) and figures were created with BioRender.com. Data normality was assessed with a Shapiro-Wilk test. All microglial density and distribution, morphology and ultrastructure data were analysed using an ordinary two-way analysis of variance (ANOVA) to compare sex hormones (ovaries *versus* testes) and genotype (FCG XX *versus* FCG XY *versus* WT). Significant two-way ANOVA tests with a main effect of sex hormones or sex chromosomes or an interaction between them were reported. Hashtags (#) were used to represent results related to a main effect of sex chromosomes while ampersands (&) were used to represent results related to a main effect of sex hormones. In cases of sex chromosome *versus* sex hormone interaction (only described *in-text* in the results section), Tukey *post-hoc* multiple comparisons test (*) was used to identify significant differences between relevant groups: FCG XX *versus* Tg XY^{-}, Tg XY^{Sry} *versus* Tg XX^{Sry}, FCG XX *versus* Tg XX^{Sry}, Tg XY^{Sry} *versus* Tg XY^{-}, FCG XX *versus* Tg XY^{Sry}, WT XX *versus* WT XY, WT XX *versus* FCG XX, WT XY *versus* Tg XY^{Sry}. Of note, some of the data sets were not normally distributed, but in the absence of a non-parametric version, we still conducted the ordinary two-way ANOVA tests. No statistical outliers were removed, and no data transformations were performed.

Data is expressed as mean ± standard error of the mean (S.E.M.). Population (N) refers to the number of animals analysed ($N = 5$ for immunofluorescence, and $N = 4$ for SEM). Sample size (n) refers to the number of imaged cells for confocal microscopy throughout the hippocampal layers per animal/condition ($n = 15$) or analysed cells for ultrastructural analysis ($n = 10–12$) to take into consideration the heterogeneity between individual cells [56, 57]. Levels of significance were set to: $^{*}p < 0.05$, $^{**}p < 0.01$, $^{***}p < 0.001$ and $^{****}p < 0.0001$.

Results

Microglial density and distribution are chromosomally and hormonally affected in the hippocampus CA1 Rad and CA1 LMol and mostly hormonally influenced in the PoDG

To better understand possible microglial variations in density and distribution due to sex chromosomes and/or sex hormones throughout the hippocampal CA1 Rad, CA1 LMol, and PoDG, we conducted immunofluorescent staining for Iba1, combined with TMEM119 and DAPI, in adulthood (P110) across the different genotypes: FCG XX (ovaries), Tg XY^{-} (ovaries), Tg XX^{Sry} (testes), Tg XY^{Sry} (testes), WT XX (ovaries), and WT XY (testes) (Fig. 1A–G").

We first analysed $Iba1^{+}/TMEM119^{+/-}$ cell density to provide insights into microglial changes at the population level. We observed a main significant chromosomal effect on total microglial density in both the Rad and LMol (Fig. 1I and J) ($F(2, 24) = 7.157$, $^{**}p = 0.0037$ and $F(2, 24) = 7.788$, $^{**}p = 0.0025$, respectively). We also detected an interaction of chromosome *versus* hormone on microglial density in these two aforementioned hippocampal layers (Rad: $F(2, 24) = 6.213$, $^{**}p = 0.0067$ and LMol: $F(2, 24) = 15.89$, $^{****}p < 0.0001$). Additionally, in the Rad we found that microglia in FCG XX mice are less numerous than in WT XX mice (XX 95.8 ± 4.5 *versus* WT XX 190.7 ± 12.3, $^{***}p = 0.0004$) while microglia in Tg XY^{Sry} mice are denser than in FCG XX mice (Tg XY^{Sry} 163.7 ± 6.3 *versus* XX 95.8 ± 4.5, $^{*}p = 0.0145$). Similar results were obtained in the LMol, where FCG XX mice again displayed less numerous microglia than WT XX mice (FCG XX 141.6 ± 7.2 *versus* WT XX 259.6 ± 16.8, $^{****}p < 0.0001$) and WT XX mice also had denser microglial cells than WT XY mice (WT XX 259.6 ± 16.8 *versus* WT XY 173.9 ± 6.8, $^{**}p = 0.0024$). In contrast, the PoDG (Fig. 1K) showed a strong main effect of hormone ($F(1,$

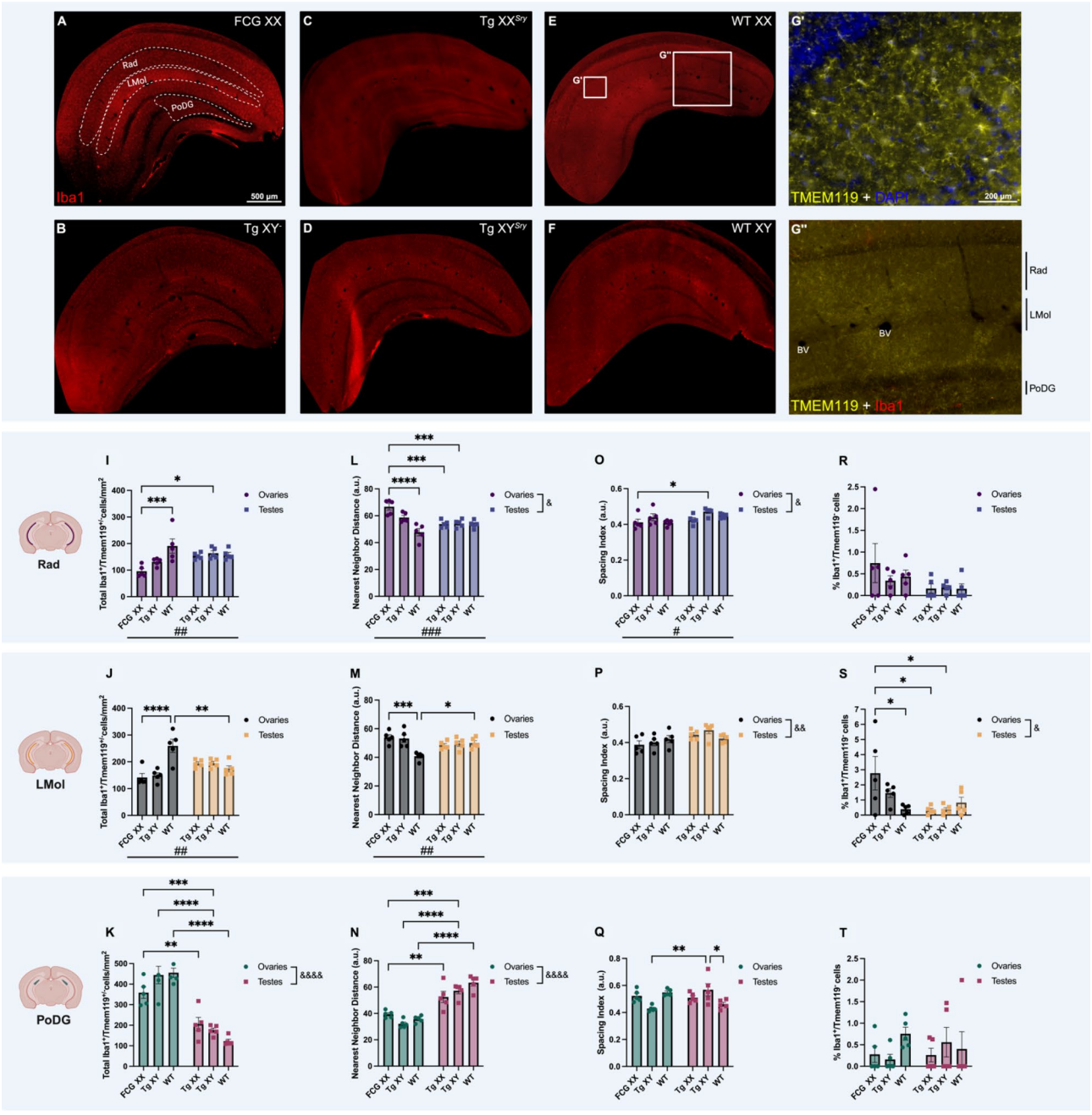

Fig. 1 Microglial density and distribution as well as peripheral cell infiltration are hormonally and chromosomally driven. Epifluorescence images of Iba1$^+$ (in red) cells at 20x of magnification in the ventral hippocampus, illustrating the examined layers: CA1 *stratum radiatum* (Rad), CA1 *stratum lacunosum-moleculare* (LMol) and dentate gyrus polymorphic layer (PoDG). Panels **A–F** show representative images from FCG XX, Tg XY$^-$, Tg XX^{Sry}, Tg XY^{Sry}, WT XX, and WT XY genotypes, respectively. Panel **G'** features a magnified area from panel **E** with zoomed-in TMEM119$^+$/DAPI $^+$ cells (in yellow and blue). Panel **G"** highlights a magnified area from panel **E**, showing Iba1$^+$/TMEM119$^+$ colocalization (in red and yellow), along with a delineation of the hippocampal layers (Rad, LMol with a few blood vessels (BV) and PoDG). Panels **I**, **J**, **and K** display the total density of Iba1$^+$/TMEM119$^{+/-}$ cells in the Rad, LMol and PoDG, respectively. Panels **L**, **M**, **and N** show the nearest neighbor distance results while panels **O**, **P**, **and Q** depict the spacing index findings. Panels **R**, **S**, **and T** represent the percentage of infiltration of Iba1$^+$/TMEM119$^-$ cells. Main sex chromosomal effects are represented by hashtags (#) while main sex hormone effects are represented by ampersands (&). Data is expressed as mean ± S.E.M., with dots representing averaged values from a single mouse ($n = 5$ mice per group). Ordinary two-way ANOVA was used to assess the interaction between sex hormones (ovaries *versus* testes) and genotype (FCG XX *versus* FCG XY *versus* WT), followed by Tukey's *post-hoc* tests for multiple comparisons in cases of significance. a.u.: arbitrary units *$p < 0.05$, **$p < 0.01$, ***$p < 0.001$ and ****$p < 0.0001$. Scale (A–F and magnifications): 500 µm and 200 µm. Created in BioRender

24) = 131.4, ****$p < 0.0001$) as well as an interaction between chromosome and hormone (F(2, 24) = 5.780, **$p = 0.0089$) on microglial density. Specifically, we found that microglia in FCG XX mice were denser than in Tg XX^{Sry} and Tg XY^{Sry} mice (FCG XX 358.7 ± 21.9 *versus* Tg XX^{Sry} 205.9 ± 18.6, **$p = 0.0059$ and Tg XY^{Sry} 175.6 ± 9.1, ***$p = 0.0008$). Additionally, microglia in Tg XY^{-} mice were denser than in Tg XY^{Sry} mice (Tg XY^{-} 444.5 ± 29.5 *versus* Tg XY^{Sry} 175.6 ± 9.1, **** $p < 0.0001$) and microglia in WT XX mice were denser than in WT XY mice (WT XX 455.5 ± 23.5 *versus* WT XY 122.4 ± 6.9, **** $p < 0.0001$).

To examine microglial distribution across the hippocampal layers, the nearest neighbor distance (NND) was measured. The NND identifies and measures the distance between a microglial cell and its closest microglia neighbor. In regions with higher cell density, the NND is typically reduced, as the cells are more closely packed together [64, 69]. In the Rad (Fig. 1L), we found main effects of both chromosomes (F(2, 24) = 13.67, ***$p = 0.0001$ and hormones (F(1, 24) = 6.422, *$p = 0.0182$) on microglial NDD, with a significant interaction between them (F(2, 24) = 12.96, ***$p = 0.0002$). The WT XX mice, which presented the densest microglia of the groups, had a significant reduction of the NND, demonstrating closer cells than in FCG XX mice, where microglia were less dense and displayed a bigger distance among cells (FCG XX 66.8 ± 1.6 *versus* WT XX 47.8 ± 1.4, **** $p < 0.0001$; Tg XX^{Sry} 53.8 ± 1.1, ***$p = 0.0006$ and Tg XY^{Sry} 54.3 ± 1.1, ***$p = 0.0010$). In the LMol (Fig. 1M), we found a main effect of chromosomes (F(2, 24) = 6.886, **$p = 0.0043$) and a significant sex chromosome *versus* hormone interaction (F(2, 24) = 9.607, ***$p = 0.0009$) on the NDD. While the WT XX mice presented the greatest microglial density, they also had a lower NND, indicating more packed cells, compared to the FCG XX and WT XY mice groups (WT XX 40.8 ± 1.8 *versus* FCG XX 53.9 ± 1.1, ***$p = 0.0004$ and WT XY 50.1 ± 0.9, *$p = 0.0164$). Lastly, in the PoDG (Fig. 1N), we obtained a strong main hormone effect (F(1, 24) = 123.5, ****$p < 0.0001$) with a sex chromosome *versus* hormone interaction (F (2, 24) = 5.131, *$p = 0.0140$) on the NDD. Hormonally female animals showed an overall greater microglial density than hormonally male animals, and consequently, they displayed a reduction of the NND. Specifically, FCG XX mice had a significant reduction of the NND compared to Tg XX^{Sry} and Tg XY^{Sry} mice (FCG XX 39.4 ± 1.1 *versus* Tg XX^{Sry} 52.5 ± 2.3, **$p = 0.0092$ and Tg XY^{Sry} 57.3 ± 1.7, ***$p = 0.0003$). Also, Tg XY^{-} had a reduction of the NND compared to Tg XY^{Sry} mice (Tg XY^{-} 32.1 ± 1.2 *versus* Tg XY^{Sry} 57.3 ± 1.7, ****$p < 0.0001$) and WT XX mice compared to WT XY mice (WT XX 35.7 ± 1.2 *versus* WT XY 64.4 ± 2.4, ****$p < 0.0001$).

The spacing index (SI), which takes into consideration the density and the NND, was also compiled to reveal the spatial organization and distribution of microglia across the hippocampal layers. In the Rad (Fig. 1O), we found a main effect of both chromosome (F(2, 24) = 4.300, *$p = 0.0254$) and hormone (F(1, 24) = 7.316, *$p = 0.0124$) on the SI, similarly to what has been previously found for the NND in the same region. Microglia in the FCG XX genotype tended to have less uniform spacing than Tg XY^{Sry} mice (FCG XX 0.4 ± 0.0 *versus* Tg XY^{Sry} 0.5 ± 0.0, *$p = 0.0352$). In the LMol (Fig. 1P), we obtained a main hormone effect (F(1, 24) = 8.894, **$p = 0.0065$) on the SI, where overall, ovary animals tended to have less uniform spacing among cells than testes animals. Lastly, in the PoDG (Fig. 1Q), we identified a sex chromosome *versus* hormone interaction (F(2, 24) = 12.84, ***$p = 0.0002$) on microglial spacing, specifically in Tg XY^{Sry} mice, which displayed more evenly spaced cells than Tg XY^{-} and WT XY mice (Tg XY^{Sry} 0.6 ± 0.0 *versus* Tg XY^{-} 0.4 ± 0.0, **$p = 0.0028$ and WT XY 0.5 ± 0.0, *$p = 0.0296$).

Together, this data indicates that the microglial population is distinctively organized among the hippocampal CA1 Rad, CA1 LMol and PoDG in a sex-specific manner. Both sex chromosomes and sex hormones appear to influence microglial density and distribution in the Rad and LMol, whereas PoDG has stronger sex hormone effects. Classically, denser microglial populations might indicate a higher level of surveillance of the brain parenchyma, although this feature has also been reported to precede a reactive state [79]. It remains undetermined what are the implications during normal physiological conditions.

Peripheral myeloid cell infiltration is overall increased in the hippocampal CA1 LMol of ovary animals

While microglia are resident immune cells of the CNS coming from the embryonic yolk sac, peripheral myeloid cells from the bone marrow, such as monocytes and macrophages, may infiltrate the brain through the vasculature and differentiate into microglia-like cells [80]. To account for this infiltration, we sought to assess the percentage of $Iba1^{+}/TMEM119^{-}$ (classified as peripheral infiltrating cells) in the aforementioned hippocampal regions of the FCG and WT adult mice (P110). In the CA1 Rad and PoDG (Fig. 1R and T), infiltration was not statistically significant. In the CA1 LMol (Fig. 1S), in contrast, a main effect of hormone was found (F(1, 24) = 6.491, *$p = 0.0177$) and a chromosome *versus* hormone interaction (F(2, 24) = 4.170, *$p = 0.0279$). Specifically, FCG XX mice had more infiltrated cells than WT XX, Tg XX^{Sry} and Tg XY^{Sry} mice (FCG XX 2.8 ± 0.6 *versus* WT XX 0.4 ± 0.1, *$p = 0.0270$; Tg XX^{Sry} 0.3 ± 0.1, *$p = 0.0218$ and Tg XY^{Sry} 0.4 ± 0.1, *$p = 0.0241$). Peripheral monocytes and macrophages were recently shown to infiltrate the brain during normal physiological conditions, in the first postnatal weeks, but their roles in the healthy adult brain

have remained undetermined [66]. Similarly, sex differences are yet to be uncovered.

Microglial morphology is shaped by a complex interaction between sex hormones and chromosomes in the hippocampal CA1 Rad and CA1 LMol, and in the PoDG

Following our microglial density and distribution investigation, we delved into microglial complex morphology in the CA1 Rad, CA1 LMol and PoDG of the adult mice (P110). The immunofluorescent staining for Iba1, DAPI and TMEM119 was examined by confocal imaging across the following genotypes: FCG XX (ovaries), Tg XY^{-} (ovaries), Tg XX^{Sry} (testes), Tg XY^{Sry} (testes), WT XX (ovaries) and WT XY (testes) mice (Fig. 2A–f"). Then, each microglial soma and arborization was manually analysed in Fiji, yielding automatic measurements for their shape: area, circularity, and solidity.

We first investigated the cellular soma of $Iba1^{+}$/$TMEM119^{+}$ microglia, where changes in shape are associated with the production of various mediators and different states [65]. An increase in soma area is commonly associated with reactive states of microglia, while a more circular soma typically reflects a surveillant state, and elongated somas suggest migration and changes in activity notably upon challenges [81]. Solidity is a measure of soma irregularity – higher solidity indicates a more convex, filled structure, while lower solidity suggests greater irregularity or rugosity [16]. Soma elongation and irregularity (reduced solidity) may correlate with enhanced phagocytic activity and increased cytokine production, showing a shift towards a more reactive microglial state [81].

In the Rad (Fig. 2G), we observed both chromosomal ($F(2, 24) = 12.37$, $^{***}p = 0.0002$) and hormonal main effects on microglial soma area ($F(1, 24) = 14.66$, $^{***}p = 0.0008$), with a significant interaction between them ($F(2, 24) = 7.845$, $^{**}p = 0.0024$). Specifically, Tg XY^{-} mice displayed a bigger soma area than Tg XY^{Sry} mice (Tg XY^{-} 52.8 ± 1.4 *versus* Tg XY^{Sry} 44.0 ± 1.3, $^{***}p = 0.0002$). In addition, in the LMol (Fig. 2H), there was a main chromosomal effect ($F(2, 24) = 10.20$, $^{***}p = 0.0006$) and a sex chromosome *versus* hormone interaction ($F(2, 24) = 3.836$, $^{*}p = 0.0358$). Interestingly, WT XX mice showed the smallest microglial soma area (WT XX 36.1 ± 0.9 *versus* FCG XX 44.0 ± 1.8, $^{*}p = 0.0213$). In contrast, in the PoDG (Fig. 2I), all groups displayed similar microglial soma area.

Next, we computed the circularity and solidity of the cellular soma, as these metrics can provide insights into the activity level and morphological changes of microglia [65]. In the Rad and PoDG (Fig. 2J and L), we obtained strong sex hormone effects (respectively, $F(1, 24) = 37.78$, $^{****}p < 0.0001$ and $F(1, 24) = 36.92$, $^{****}p < 0.0001$) in the circularity of the soma, where, overall, hormonally male animals had a more circular soma, and hormonally female animals a more elongated soma. Similarly in the LMol (Fig. 2K), for soma circularity, we found a strong hormone effect ($F(1, 24) = 27.24$, $^{****}p < 0.0001$) and lighter chromosomal effect for the soma circularity ($F(2, 24) = 6.898$, $^{**}p = 0.0043$), with an interaction between them ($F(2, 24) = 4.379$, $^{*}p = 0.0239$), whereby overall testes animals tended to display more circular somas then ovary animals. More specifically, FCG XX showed a more elongated soma than WT XX and Tg XX^{Sry} (FCG XX 0.7 ± 0.0 *versus* WT XX 0.8 ± 0.0, $^{*}p = 0.0142$ and Tg XX^{Sry} 0.8 ± 0.0, $^{***}p = 0.0004$).

In regard to microglial soma solidity, again, in the Rad and PoDG (Fig. 2M and O), we observed a strong main hormone effect (respectively, $F(1, 24) = 39.60$, $^{****}p < 0.0001$ and $F(1, 24) = 24.66$, $^{****}p < 0.0001$), where animals with ovaries exhibited a more rugous soma, while animals with testes generally displayed a more convex soma. Similarly, in the LMol (Fig. 2N), we also found a main hormone effect for microglial soma solidity ($F(1, 24) = 17.24$, $^{***}p = 0.0004$) with the addition of a chromosome effect ($F(2, 24) = 5.396$, $^{*}p = 0.0116$) with a significant interaction ($F(2, 24) = 3.677$, $^{*}p = 0.0404$). Specifically, FCG XX mice demonstrated a more rugous microglial soma shape than Tg XX^{Sry} mice, which displayed a more convex microglial soma morphology (FCG XX 0.9 ± 0.0 *versus* Tg XX^{Sry} 1.0 ± 0.0, $^{**}p = 0.0071$).

Secondly, we investigated possible changes in the arborization of microglia, notably linked to their surveillance of the parenchyma and their other physiological roles [65, 82]. Typically, surveillant microglia portrait longer, circular and ramified branching – characterized by more circularity and reduced solidity. Reactive microglia often suffer a loss of ramification, becoming more amoeboid – hence portraying more solidity, as they fill more area in space. Elongated shapes, known as rod microglia, represent a state often seen in injuries/pathology, as well as during aging [81].

To begin with, the Rad (Fig. 2P) was the only region to exhibit a primary main chromosomal effect ($F(2, 24) = 4.832$, $^{*}p = 0.0172$) in microglial arborization area. Specifically, microglia had a significantly smaller arborization area in FCG XX mice than Tg XY^{Sry} mice (FCG XX 1979.9 ± 94.7 *versus* Tg XY^{Sry} 2796.8 ± 92.9, $^{*}p = 0.0475$). In turn, LMol (Fig. 2Q) demonstrated a main hormone effect ($F(1, 24) = 4.418$, $^{*}p = 0.0462$) with ovary-carrier animals displaying an overall decrease in microglial arborization area compared to testes animals. In the PoDG (Fig. 2R), microglia had a similar arborization area across genotypes.

Next, microglial arborization circularity was found to present a sex chromosome by hormone interaction in all the examined hippocampal layers. In the Rad ($F(2, 24) = 7.847$, $^{**}p = 0.0024$) a stronger difference was found

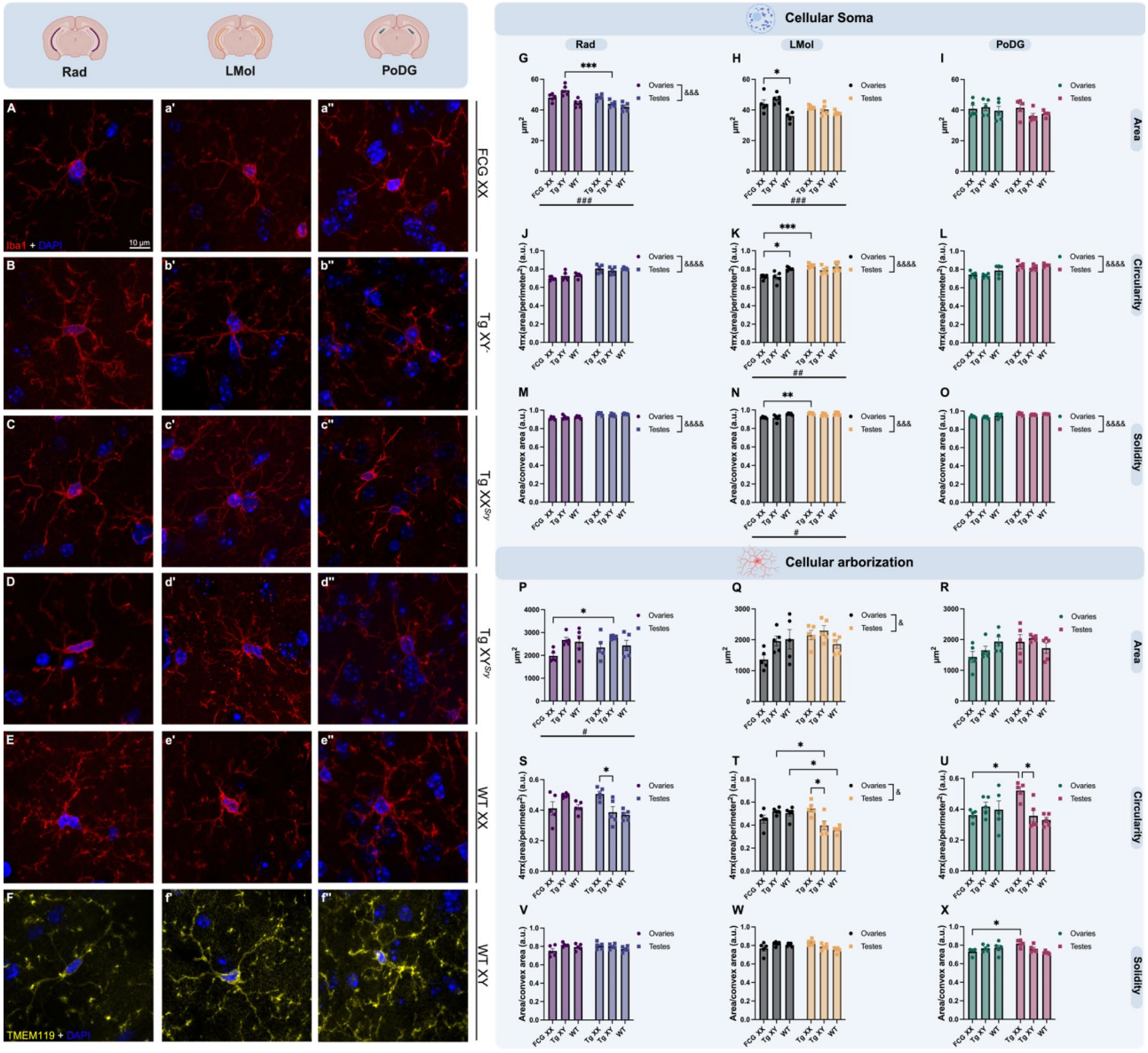

Fig. 2 Microglial morphology is affected by a complex interaction between sex hormones and sex chromosomes. Confocal images of Iba1$^+$/DAPI$^+$ (**in red and blue; A–e″**) or TMEM119$^+$/DAPI$^+$ (**in yellow and blue; F–f″**) cells at 63x of magnification from the CA1 *stratum radiatum* (Rad; **A–F**), CA1 *stratum lacunosum-moleculare* (LMol; **a′–f′**) and dentate gyrus polymorphic layer (PoDG; **a″–f″**). Genotypes (FCG XX, Tg XY$^-$, Tg XX^{Sry}, Tg XY^{Sry}, WT XX and WT XY mice) are shown across the examined layers in A–a″, B–b″, C–c″, D–d″, E–e″, F–f″, respectively. Panels **G**, **H**, **and I** display the soma area; panels **J**, **K**, **and L** represent the soma circularity index and, panels **M**, **N**, **and O** present the cell soma solidity in the Rad, LMol and PoDG, respectively. Panels **P**, **Q and R** display the cellular arborization area; panels **S**, **T and U** show the cellular arborization circularity index and, panels **V**, **W and X** depict the arborization solidity results in the Rad, LMol and PoDG, respectively. Main sex chromosomal effects are represented by hashtags (#) while main sex hormone effects are represented by ampersands (&). Data is expressed as mean ± S.E.M., with dots representing averaged values from a single mouse ($n = 15$ cells in $N = 5$ mice per group). Ordinary two-way ANOVA was used to assess the interaction between sex hormones (ovaries *versus* testes) and genotype (FCG XX *versus* FCG XY *versus* WT), followed by Tukey's *post-hoc* test for multiple comparisons. a.u.: arbitrary units $^*p < 0.05$, $^{**}p < 0.01$, $^{***}p < 0.001$ and $^{****}p < 0.0001$. Scale (A–f″): 10 µm. Created in BioRender

between Tg XX^{Sry} and Tg XY^{Sry} mice (Fig. 2S), where the first presented a more circular morphology than the second (Tg XX^{Sry} 0.5 ± 0.0 *versus* Tg XY^{Sry} 0.4 ± 0.0, $^*p = 0.0406$). In addition to presenting a sex chromosome *versus* hormone interaction (F (2, 24) = 11.26, $^{***}p = 0.0004$), the LMol (Fig. 2T) also displayed a main hormone effect (F (1, 24) = 6.710, $^*p = 0.0160$). Specifically, the Tg XY^{Sry} genotype presented microglia with a more elongated arborization than Tg XX^{Sry} and Tg XY$^-$ mice (Tg XY^{Sry} 0.4 ± 0.0 *versus* Tg XX^{Sry} 0.5 ± 0.0, $^*p = 0.0107$, and Tg XY$^-$ 0.5 ± 0.0, $^*p = 0.0408$). Additionally, microglia in WT XX mice had a significantly

more circular arborization than in WT XY mice (WT XX 0.5 ± 0.0 *versus* WT XY 0.4 ± 0.0, $^{*}p = 0.0136$). In the PoDG (Fig. 2U), there was a sex chromosome *versus* hormone interaction ($F(2, 24) = 7.168$, $^{**}p = 0.0036$), where again the Tg XY^{Sry} genotype showed a more elongated microglial arborization shape, while the Tg XX^{Sry} genotype displayed an increase in circular morphology (Tg XY^{Sry} 0.4 ± 0.0 *versus* Tg XX^{Sry} 0.5 ± 0.0, $^{*}p = 0.0240$, and XX 0.4 ± 0.1, $^{*}p = 0.0306$).

We lastly assessed the arborization solidity, which revealed a significant sex chromosome *versus* hormone interaction in the Rad, LMol and PoDG (Fig. 2V, W and X, and respectively $F(2, 24) = 3.492$, $^{*}p = 0.0466$; $F(2, 24) = 7.465$, $^{**}p = 0.0030$ and $F(2, 24) = 7.166$, $^{**}p = 0.0036$). Of note, in the Rad and LMol, none of the relevant groups were pointed out by the *post-hoc* test. However, in the PoDG, FCG XX mice showed a decreased solidity in comparison to Tg XX^{Sry} mice (FCG XX 0.7 ± 0.0 Tg XX^{Sry} 0.8 ± 0.0, $^{*}p = 0.0320$).

Together, this data suggests that microglial morphology is influenced by a complex interaction between sex hormones and chromosomes across the hippocampal CA1 Rad, CA1 LMol and PoDG. Cells portraying smaller cellular somas in addition to extensive and well-branched processes are usually linked to a surveillant state of microglia, whereas the shrinkage of processes and bigger somas are usually linked to reactive states [83–86]. It remains to be discovered what these features mean during normal physiological conditions.

Microglial ultrastructural markers of cellular stress are primarily influenced by sex chromosomes in the hippocampus CA1 Rad

To investigate the hormonal and chromosomal effects on microglial ultrastructure, we conducted SEM in the CA1 Rad of adult mice (P110), where we observed strong main effects of sex chromosomes in mice from the different genotypes: FCG XX (ovaries), Tg XY^{-} (ovaries), Tg XX^{Sry} (testes), Tg XY^{Sry} (testes), WT XX (ovaries), and WT XY (testes) (Fig. 3A–f'). We examined microglial cell bodies, identifying them based on their Iba1 staining and/or classical ultrastructural microglial features.

Our analysis revealed that microglial cell bodies in WT mice make overall more contacts with pre- and post-synaptic elements than in FCG mice. The number of microglial contacts with pre-synaptic terminals (Fig. 3G) showed a strong main effect of chromosome ($F(2, 266) = 7.893$, $^{***}p = 0.0005$). Specifically, the WT XY mice had almost double counts of microglial contacts with these elements than the Tg XY^{Sry} mice (WT XY 5.2 ± 0.4 *versus* Tg XY^{Sry} 3.0 ± 0.3, $^{***}p = 0.0008$). However, microglial contacts with post-synaptic elements (Fig. 3H) seemed to rely on a main sex hormone effect ($F(1, 266) = 6.397$, $^{**}p = 0.0120$), with a weak interaction between sex hormones and chromosomes ($F(2, 266) = 3.246$, $^{*}p = 0.0405$). Interestingly, microglia in the WT XY mice made more contacts with post-synaptic elements than the WT XX mice (WT XY 1.8 ± 0.2 *versus* WT XX 0.95 ± 0.1, $^{*}p = 0.0196$).

Our analysis of microglial cell bodies further revealed that multiple ultrastructural markers of cellular stress are primarily influenced by sex chromosomes. When analysing the numbers of healthy ER/Golgi cisternae (Fig. 3I), we found a main chromosome effect ($F(2, 266) = 20.04$, $^{****}p < 0.0001$) and a sex chromosome *versus* hormone interaction ($F(2, 266) = 4.482$, $^{*}p = 0.0122$). Specifically, the Tg XY^{-} mice had more microglial ER/Golgi counts than FCG XX mice (Tg XY^{-} 22.5 ± 2.3 *versus* FCG XX 12.3 ± 1.3, $^{***}p = 0.0002$). After measuring the intracisternal distance of these ER/Golgi (Fig. 3J; dilatation > 100 nm), we found that this feature was also primarily affected by sex chromosomes ($F(2, 266) = 3.826$, $^{*}p = 0.0230$) and was especially higher in FCG XX mice than in WT XX mice (FCG XX 0.8 ± 0.2 *versus* WT XX 0.1 ± 0.0, $^{*}p = 0.0166$). Similarly, microglial extracellular digestion (Fig. 3K) was affected by hormones ($F(1, 264) = 4.420$, $^{*}p = 0.0365$), but mainly by chromosomes ($F(2, 264) = 12.27$, $^{****}p < 0.0001$). Interestingly, this feature was higher in the Tg XY^{Sry} genotype than the FCG XX and Tg XX^{Sry} groups (Tg XY^{Sry} 0.9 ± 0.1 *versus* FCG XX 0.3 ± 0.0, $^{**}p = 0.0039$, and Tg XX^{Sry} 0.3 ± 0.1, $^{*}p = 0.0153$).

The abundance of dystrophic mitochondria (Fig. 3L; presenting abnormal cristae structure or vacuoles) in microglial cell bodies also showed a main effect of chromosomes ($F(2, 266) = 3.087$, $^{*}p = 0.0473$) and sex hormones ($F(1, 266) = 6.911$, $^{**}p = 0.0091$), with microglia from testes animals having overall higher counts of this altered organelle. Similarly, differences in microglial elongated mitochondria (Fig. 3M; elongation in length > 1000 nm) were mostly chromosomally driven ($F(2, 266) = 3.060$, $^{*}p = 0.0486$). The abundance of microglial immature lysosomes (Fig. 3N; both primary and secondary lysosomes) also presented only a main sex chromosome effect ($F(2, 266) = 4.823$, $^{**}p = 0.0088$).

While microglial empty phagosomes (Fig. 3O) displayed a main hormone effect ($F(1, 262) = 4.619$, $^{*}p = 0.0325$) with ovary animals having higher counts, filled phagosomes (Fig. 3P) showed a main chromosome effect ($F(2, 266) = 4.690$, $^{**}p = 0.0100$). Lastly, microglial tertiary lysosomes (Fig. 3Q) showed a sex chromosome *versus* hormone interaction ($F(2, 266) = 4.844$, $^{**}p = 0.0086$), where interestingly, WT XX mice had more microglial tertiary lysosomes build up than WT XY mice (WT XY 0.1 ± 0.0 *versus* WT XX 0.6 ± 0.1, $^{*}p = 0.0125$).

Together, the data show a sex chromosomal dependency in order to shape markers of cellular stress in microglial cells. Increased contacts with pre- and post-synaptic elements in the WT group might indicate

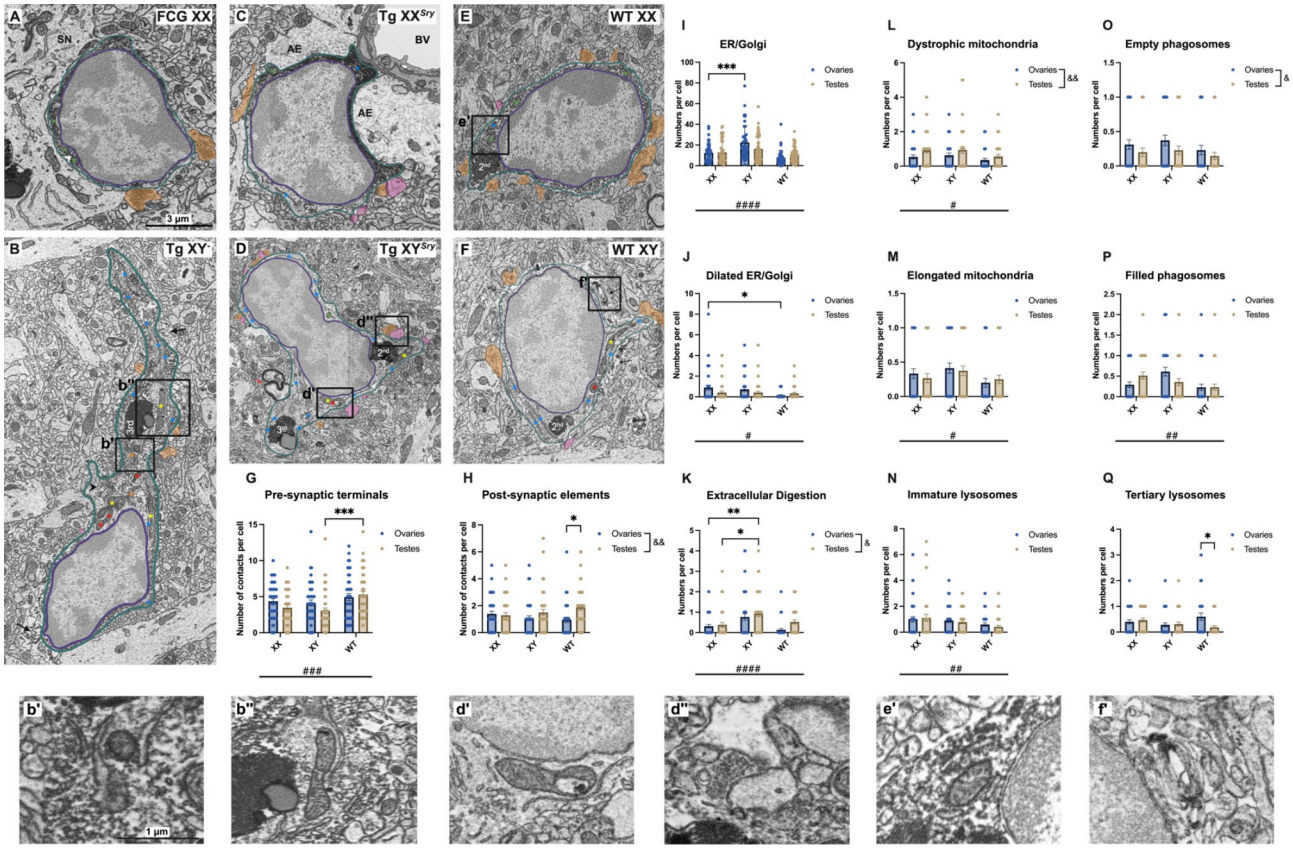

Fig. 3 Microglial ultrastructural markers of cellular stress are mostly chromosomally driven. Scanning electron microscopy images of microglial cell bodies featuring Iba1$^+$ staining (**A**, **B**, **C**, **and E**) and non-stained microglial cell bodies (**D and F**) in the CA1 *stratum radiatum* (Rad). Genotypes (FCG XX, Tg XY$^-$, Tg XX^{Sry}, Tg XY^{Sry}, WT XX, and WT XY mice) are shown in panels **A–F**, respectively. Panels **b'** and **b"** show a magnified view of the areas in **B** (dilated endoplasmic reticulum (ER)/Golgi apparatus and an elongated mitochondrion). Panels **d' and d"** show a magnified view of the areas in **D** (elongated and dystrophic mitochondrion, and pre- and post-synaptic elements). Panel **e'** shows a magnified view of the area in **E** (healthy mitochondria). Panel **f'** shows a magnified view of the area in **F** (extracellular digestion). Panels **G** and **H** represent the contacts with pre- and post-synaptic elements, respectively. Panel **I** displays the numbers of ER/Golgi while panel **J** displays dilated ER/Golgi (> 100 nm) numbers. Panel **K** presents the number of extracellular digestion events. Panel **L** shows the numbers of dystrophic mitochondria and panel **M** the numbers of elongated mitochondria (> 1000 nm). Panel **N** shows the numbers of immature lysosomes (primary and secondary lysosomes summed). Panel **O** depicts the numbers of empty phagosomes and panel **P** the numbers of filled phagosomes per cell. Lastly, panel **Q** represents the numbers of tertiary lysosomes. **Purple outline** = nuclear membrane; **turquoise outline** = cytoplasmic membrane; **green asterisk** = healthy mitochondria; **blue asterisk** = ER/Golgi; **orange asterisk** = dilated ER/Golgi; **yellow asterisk** = elongated mitochondria; **red asterisk** = dystrophic mitochondria; **black arrowhead** = filled phagosome; **white arrowhead** = empty phagosome; **black arrow** = extracellular digestion area; **red arrow** = contact with a myelinated axon; **orange pseudo-coloring** = contact with a pre-synaptic terminal; **pink pseudo-coloring** = contact with a post-synaptic element; **SN** = satellite neuron; **BV** = blood vessel; **AE** = astrocytic-endfeet; **1st** = primary lysosome; **2nd** = secondary lysosome; **3rd** = tertiary lysosome. Main sex chromosomal effects are represented by hashtags (#) while main sex hormone effects are represented by ampersands (&). Data is expressed as mean ± S.E.M., with dots representing absolute cell values (n = 10–12 cells in N = 4 mice per group). Ordinary two-way ANOVA was used to assess the interaction between sex hormones (ovaries *versus* testes) and genotype (FCG XX *versus* FCG XY *versus* WT), followed by Tukey's *post-hoc* test for multiple comparisons. *$p < 0.05$, **$p < 0.01$, ***$p < 0.001$ and ****$p < 0.0001$. Scales (A–F and magnifications): 3 µm and 1 µm. Created in BioRender

enhanced synapse plasticity and maintenance, as microglia are known to constantly modulate synapses during normal physiological conditions [14, 24, 87].

Microglial ultrastructural nuclear and cytoplasmic membrane circularity as well as solidity are sex chromosomally affected in the hippocampus CA1 Rad

We lastly investigated microglial nuclear and cytoplasmic morphology at the ultrastructural level using SEM imaging in the hippocampus CA1 Rad of adult mice (P110). All genotypes were analysed, but the differences were more pronounced between the Tg XY^{Sry} (testes) and WT XY (testes) mice (Fig. 4A and B).

Our analysis showed that microglial nuclear membrane circularity (Fig. 4C) is influenced by a main chromosome effect ($F(2, 267) = 5.514$, **$p = 0.0045$). Specifically, microglia in the Tg XY^{Sry} genotype had their nuclear membrane circularity reduced in comparison to WT XY mice (Tg XY^{Sry} 0.7 ± 0.0 *versus* WT XY 0.8 ± 0.0, *$p = 0.0222$).

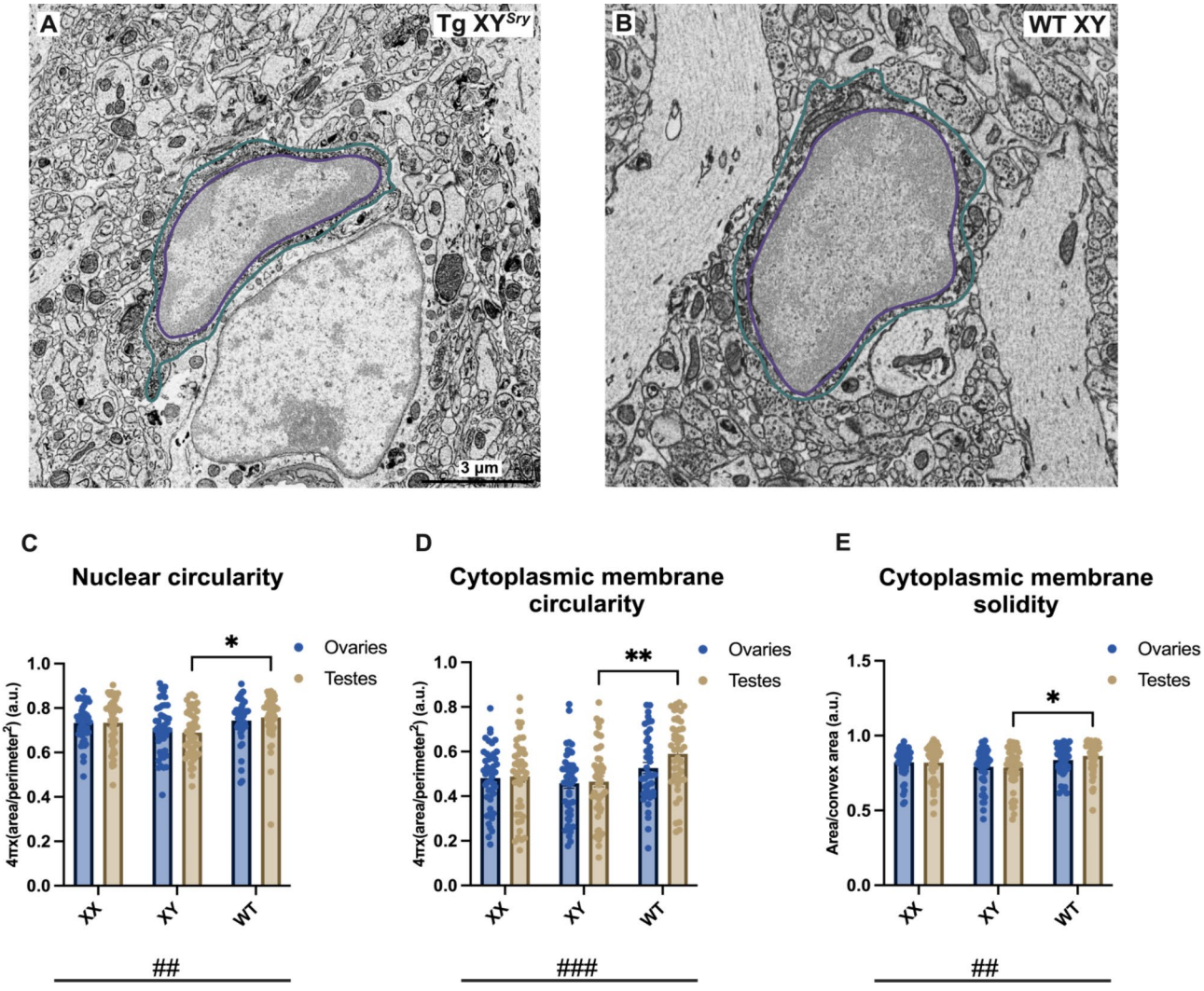

Fig. 4 Nuclear and cytoplasmic membrane circularity and solidity are sex chromosomally affected at the ultrastructural level. Scanning electron microscopy images of microglial cell bodies featuring positive Iba1 staining (**A and B**) in the CA1 *stratum radiatum* (Rad). Genotypes Tg XY^{Sry} and WT XY are shown in panels **A and B**, respectively. Panel **C** shows the nuclear circularity while panels **D and E** depict the cytoplasmic membrane circularity and solidity, respectively. **Purple outline** = nuclear membrane; **turquoise outline** = cytoplasmic membrane. Main sex chromosomal effects are represented by hashtags (#) while main sex hormone effects are represented by ampersands (&). Data is expressed as mean ± S.E.M., with dots representing absolute cell values (n = 10–12 cells in N = 4 mice per group). Ordinary two-way ANOVA was used to assess the interaction between sex hormones (ovaries *versus* testes) and genotype (FCG XX *versus* FCG XY *versus* WT), followed by Tukey's *post-hoc* tests in cases of significance for multiple comparisons. *$p < 0.05$, **$p < 0.01$, ***$p < 0.001$ and ****$p < 0.0001$. Scale: 3 µm. Created in BioRender

Similarly, the cytoplasmic membrane circularity and solidity (Fig. 4D and E) were influenced by sex chromosomes (respectively, $F(2, 267) = 9.183$, ***$p = 0.0001$ and $F(2, 267) = 6.182$, **$p = 0.0024$). Interestingly, microglia in the Tg XY^{Sry} genotype had their cytoplasmic membrane circularity and solidity significantly reduced compared to WT XY mice (Circularity: Tg XY^{Sry} 0.5 ± 0.0 *versus* WT XY 0.6 ± 0.0, **$p = 0.0018$; Solidity: Tg XY^{Sry} 0.8 ± 0.0 *versus* WT XY 0.9 ± 0.0, *$p = 0.0160$). Our confocal analysis above provided similar results in the Tg XY^{Sry} mice, where microglia presented a more elongated arborization in comparison to the Tg XX^{Sry} mice.

Discussion

Our study investigated the effects of sex hormones *versus* sex chromosomes on multiple microglial features during normal physiological conditions. We used the FCG mouse model to assess the outcomes of sex hormones unrelated to sex chromosomes, and vice versa, in the ventral hippocampus CA1 Rad and CA1 LMol as well as in the PoDG. We began by analysing microglial density and distribution to gain insights into the population-level characteristics of microglia, which revealed notable sex differences in previous studies [64]. Next, we examined microglial complexity, now focusing on individual cells, to understand the shape of the cellular soma and

arborization. This analysis provides insight into microglial function across contexts of health and disease [57, 84]. Traditionally, less branched microglia, with enlarged somas and higher circularity coupled with enhanced solidity are classified as reactive, while more highly ramified, with smaller somas and reduced solidity are considered surveillant microglia [83–86]. However, microglia display a broad spectrum of morphologies, ranging from hyper-ramified forms in response to stress [88], to senescent, dark and dystrophic phenotypes in stress, aging and disease [28, 77, 89, 90]. Finally, we explored microglia at a super-resolution level by examining their ultrastructure. This analysis not only highlights how microglia interact with other cells and elements in the brain parenchyma, such as pre- and post-synaptic elements, blood vessels, astrocytes and neurons, but also reveals the health or dystrophic state of their organelles, providing evidence of cellular stress for instance [38, 91].

It is important to note that sex determination and differentiation are important processes for the brain, body and immunity. First, sex determination takes place during fertilization, which is led by genes located on the sex chromosomes. These chromosome complements, XX in females (with one X inactivated) and XY in males, carry important genes for starting the sex-differentiation of the brain and body [10, 92]. Sex differentiation is guided by a network of genes and sex hormones (or sex steroids) – specifically, androgens and estrogens – exerting effects on the brain, body, and behavior [10, 13, 15, 93]. In fact, the X chromosome plays a crucial role in carrying important genes mediating immune function, which may partially explain the sexual dimorphism observed in the immune system [94, 95]. Notably, in Cx3cr1-NuTRAP (short of C-X3-C motif chemokine receptor 1-nuclear tagging and translating ribosome affinity purification) and WT mice, where hippocampal $Cd11b^{+}$ microglia were sorted, most of the differently expressed genes (DEGs) between 5–6-month-old male and female mice were found in the sex chromosomes [96]. The researcher found that these DEGs were primarily female-biased and were enriched in senescent and disease-associated microglial signatures in aged mice (22–25-month-old). Upstream regulators, such as inflammatory cytokines that include tumor necrosis factor (TNF), interleukin 1-beta (IL-1β) and interferon-gamma (IFNγ), were also found to be upregulated in aged female mice [96]. In addition to the effects of sex chromosomes, sex hormones influence the brain and behavior throughout life and microglia are crucial during this process [97]. In newborn rat pups (P0–P1), males presented twice as many $Iba1^{+}$ amoeboid-shaped microglia than females in the POA [18]. By administrating minocycline in the newborn pups, thus affecting microglia in early postnatal life, these sex differences previously reported were prevented [18]. In addition, the administration of estradiol postnatally (P0–P1) in female rats, showed that this hormone was able to promote a masculinization-like effect, increasing microglial counts to the levels found in males [18]. However, the modulation of microglia with minocycline prevented this masculinizing effect in the POA in estradiol-treated female mice. Later, in adulthood (P65), estradiol treatment in gonadectomized female rats could promote a male-like copulatory behavior. Moreover, an increase in the dendritic spines (by the detection of spinophilin protein) could also be rescued with estradiol treatment, albeit co-treatment with minocycline could not [18]. This indicates that microglia are highly affected by both sex hormones and sex chromosomes, and are needed during development and adulthood to shape neuronal circuits and modulate behavior.

In our first analysis of the hippocampal CA1 Rad and CA1 LMol, and of the PoDG, we observed that microglial density and distribution in adult mice were significantly influenced by both sex hormones and chromosomes. In fact, in the Rad and LMol, there was a clear interaction between sex hormones and chromosomes, while in the PoDG, the effects were primarily driven by sex hormones. In particular, we found an intriguing discrepancy in density between the WT XX and FCG XX mice. In contrast, microglia in the FCG XX genotype were less dense than in Tg XY^{Sry} mice, showing a sex difference in density. Correspondingly, FCG XX mice exhibited a higher NND, while WT XX microglia showed a reduction of their NND.

In the PoDG, mice with ovaries showed denser microglial populations with overall closer cells compared to mice with testes. Overall, mice with ovaries had a less uniform microglial spacing than animals with testes. To our knowledge, we are the first ones to demonstrate this main hormonal effect on microglial density and distribution, particularly in the PoDG, while in the CA1 Rad and CA1 LMol there was an interaction between sex chromosomes and hormones. The DG is known to extensively express estrogen receptors alpha and beta (ERα and β). In the DG of adult male rats (P70), both ERα and β were colocalized with markers of proliferating cells (such as Ki-67 antigen) and differentiated newly formed neurons (doublecortin; DCX) [98]. This suggests that estrogen may play a key role in mediating cell survival in this region, which might explain the strong main effects of sex hormones, especially in the PoDG, where we showed that animals with ovaries displayed a greater microglial density. Importantly, comparable levels of sex hormones have been reported in both ovaries and testes FCG groups. Both Tg XX^{Sry} and Tg XY^{Sry} genotypes display similar testosterone levels during adulthood [99]. Likewise, FCG XX and Tg XY^{-} presented little to no difference in their pubertal timing or estrous cycle [9, 49, 100, 101].

In addition to region-specific changes, our study highlights microglial sex differences in the ventral hippocampus at large, since the Tg XY^{Sry} mice showed increased microglial density, NND and spacing index in comparison with the FCG XX genotype. Other studies using WT mice in adulthood (around P90), also reported that males had a greater density of Iba1$^+$ cells than their female counterparts in the hippocampus during normal physiology [18, 44]. Similarly, after cortical injury (sagittal cut through the neocortex and corpus callosum), adult male CD1 mice (around P60) presented a greater density of Iba1$^+$ cells near the wound [102]. However, it is important to note that microglial sex differences are highly dependent on age, context, region, and species [10, 13, 15, 93]. Contrasting the results in mice, in adult rats (ranging from P55 to P65), females were reported to have a greater density of Iba1$^+$ cells in the hippocampus (specifically in the CA1 and DG) [17]. Moreover, in the hippocampus of adult male and female rats (around P90), no difference of Iba1$^+$/TMEM119$^+$ cell density was found by Sharon and colleagues [59]. Of note, Guneykaya et al. have not specified the hippocampal layer in which the analysis was conducted nor controlled for the estrous cycle [44]. In contrast, Schwarz and Acaz-Fonseca et al. reported that the mice or rats were in the estrous phase [17, 102]. Moreover, Acaz-Fonseca and colleagues also stated that the estrous cycle did not significantly influence the results [17]. All of these factors are important considerations when analysing sex differences.

We also noted very few differences between our WT XX and WT XY mice. Particularly, for our density results, in the CA1 LMol, the WT XX mice showed increased microglial density compared to the WT XY mice. Our microglial ultrastructure analyses also revealed more contacts with post-synaptic elements in WT XY mice, while WT XX mice had more tertiary lysosome counts per cell. Other than that, the WT genotype did not have other differences. The microglial sex differences debate is still ongoing, as described above, and some research on physiological conditions in mice showed that males have denser microglia in hippocampal regions than female counterparts [44, 102]. In rats, some studies revealed the opposite or even no microglial density difference between sexes [17, 59]. The particular hippocampal pole, region and layer examined might be behind some of these differences, in addition to possible variations between species. For instance, a study by De Felice and colleagues recently showed in adult (8–12 weeks old) male mice that the dorsal and ventral pole of the hippocampus CA1 Rad present differences in microglial density, morphology, and ultrastructure [56]. Interestingly, the dorsal pole was found to house more microglia in both male and female adult mice, however, the ventral pole had microglia with bigger soma and arborization perimeter [56, 103]. This exemplifies that different hippocampal poles might have different microglial states [56, 103].

We further observed a decrease in microglial density in the FCG XX genotype compared to WT female mice in the CA1 Rad and CA1 LMol, as well as decreased soma area and increased soma circularity, particularly in the LMol. This was intriguing because the FCG XX mice do not bear a transgene, and thus should be genetically identical to WT females. As is the case for the other FCG progeny, FCG XX mice have a Tg XY$^-$ male as a sire; it is possible that this confers them an epigenetic signature that might account for the observed phenotypic differences between FCG XX mice and WT females. Another important factor to be considered is the estrous cycle or increased hormonal fluctuations in the FCG XX, as elevated estradiol levels in the proestrus phase are associated with increased neuronal excitability and can modulate microglial activity and cytokine production [104, 105]. Additional limitations from this model should also be addressed. Generally, the Tg XX^{Sry} mice have smaller testes and lack sperm in comparison with the Tg XY^{Sry}. Similarly, Tg XY$^-$ mice lose germ cells, portrait smaller ovaries and stop their estrous cycling earlier, making both Tg XX^{Sry} and XY$^-$ mice less fertile [99]. Thus, while the FCG model is a powerful tool for studying sex differences in multiple contexts [42, 43], studying the contribution of these additional variables may be necessary to develop a nuanced perspective on the contribution of sex hormones and sex chromosomes to (patho)physiology. We also acknowledge that most FCG studies employ a 2×2 ANOVA [42, 43, 106, 107]. We have decided to add the WT as a point of reference, as this had not been done previously.

Very recently, a study by Panten and colleagues demonstrated that a 3.2 MB region of the X chromosome was spontaneously translocated to the Y chromosome with the *Sry* deletion (Y^{Sry-}) in the strain 010905 from Jackson Laboratories [108]. This mutation caused a 2-fold upregulation of several X-linked genes, including *Tmsb4x*, *Tlr8*, *Tlr7*, *Prps2*, *Frmpd4*, *Msl3*, *Arhgap6*, *Amelx* and *Hccs* in the Tg XY$^-$ and Tg XY^{Sry} genotypes [108]. Although microglia were not assessed specifically, it is widely known that Toll-like receptors (TLRs) are of extreme importance for the innate immune function of microglia, including the recognition of pathogen-associated molecular patterns (PAMPs) [109, 110]. This mutation could thus have possibly augmented and exacerbated some microglial responses we observed. For instance, as we see some elevated signs of cellular stress (e.g., ER/Golgi dilation and extracellular digestion) in both Tg XY genotypes, this unexpected mutation could have influenced these findings. We acknowledge that other possible interpretations of our results might be considered due to this very recent report, and we hope that future research

will focus on the investigation not only on Y^{Sry-} affected genotypes, but also on the FCG XX and XX^{Sry}.

Of note, our density and morphometric analysis can provide an estimate of the cellular density and complexity of microglia, but, as with any other analyses of this kind, it is worth mentioning that it gives an estimation of cell counts and shape descriptors. However, overall, it provides great insights into this cellular population organization and possible functions, as previously shown [16, 56, 58]. Additionally, using unbiased stereological approaches would be recommended in future studies to provide precise information on the changes in microglial density across the entire examined regions in 3D [111]. It will also be important for future research to dive deeper into molecular approaches to reveal the mechanisms driving these chromosomic and hormonal changes in microglia. Moreover, comparing the density of other cellular elements (such as $DAPI^+$ cells) relative to microglia will be crucial for examining possible structural changes and adding another layer of complexity to our understanding of microglial distribution in relation to other cell types.

Furthermore, we have observed an increased infiltration of $Iba1^+/TMEM119^-$ myeloid cells in the CA1 LMol in the FCG XX group compared to the WT XX, Tg XX^{Sry}, and Tg XY^{Sry}, and, overall slightly higher levels in animals with ovaries. Estrogen is known for its protective effects on the neuro-vasculature, particularly in women. Although both men and women express ERα and ERβ receptors in their vasculature, the mechanisms underlying the greater cardioprotective effects in women remain unclear [112–114]. Notably, ovariectomy (OVX) has been shown in multiple studies to result in increased blood-brain barrier (BBB) permeability compared to non-OVX rodents [115, 116]. Additionally, in aged OVX female rats (9–11 months old), a 2- to 4-fold increase in BBB permeability in the hippocampus was observed compared to younger OVX females (4 months old) [116]. One of the key functions of the BBB is to regulate the entrance of lymphocytes into the brain [5]. In a brain inflammation model induced by TNFα and IFNγ, the treatment of a transmigration human brain endothelial cell (hCMEC/D3) system with estradiol significantly attenuated lymphocyte infiltration [115]. Remarkably, the LMol is a good source of blood supply in the CA1 (see BVs in Fig. 1G") [33]. We hypothesize that in physiological conditions, the infiltrating cells had easier access from the blood to the hippocampus via the LMol in animals with ovaries. It should also be noted that TMEM119 has been pointed as a reliable microglia-specific marker during normal physiological conditions, at least during adulthood [66, 117–119]. However, another alternative interpretation could be that microglial expression of TMEM119 is context-dependant, meaning that these cells can downregulate TMEM119, as previously shown during exacerbated brain inflammation or neurodegeneration such as Alzheimer's disease pathology [120, 121]. In particular, lipopolysaccharide-induced microglia ($CD45^{int}/CD11b^{pos}$ FACS sorted) from adult (between 6 and 8 weeks) Tmem119-eGFP mice had a significantly reduced Tmem119 gene and protein expression, especially in the midbrain, followed by the cortex and cerebellum [119].

Moreover, we found that microglial morphology was shaped by the interaction of sex hormones and chromosomes in the CA1 Rad and CA1 LMol, with hormonal effects being predominant in the PoDG. Larger microglial somas are usually indicative of a more reactive state (as seen in both Rad and LMol of Tg XY^- and FCG XX mice, respectively). While functional implications during normal physiological conditions remain unclear, this morphological change can indicate a higher metabolic activity during phagocytosis [83, 111, 122]. In contrast, smaller somas are indicative of a surveillant state in microglia (as seen in the Rad of Tg XY^{Sry} mice and LMol of WT XX mice) [18, 111]. We observed that microglia in FCG XX mice displayed a decreased soma circularity and solidity resulting in an overall bigger, more elongated and less rugous cellular soma compared to WT XX and Tg XX^{Sry} mice. Classically, extensive branching can be related to more surveillant states of microglia as seen in the CA1 Rad, whereas Tg XY^{Sry} mice had a bigger arborization area than FCG XX mice [70, 85, 123, 124]. Interestingly, across all examined layers, Tg XX^{Sry} displayed increased circularity, while other testes-bearing mice showed a reduction in this feature. Sex differences were already reported in microglial morphology during normal physiology. Using mice in adulthood (around P90), Guneykaya and colleagues showed that adult (P91) male WT mice not only have a higher density of $Iba1^+$ cells in the hippocampus compared to counterpart females, but also exhibit more ramified microglia with larger cell somas [44]. Supporting the view that microglia are context-dependent, a study in adult rats (P55-65) found the opposite: females exhibited higher microglial density, along with thicker and longer processes in the CA1 and DG regions [17]. Our observed differences in cell morphology could be driven by the aforementioned factors. In addition, we provide new insights into the complex interaction between sex hormones and chromosomes in modulating microglial morphology across different hippocampal layers – a level of detail that has not been previously explored.

Finally, we observed that microglial ultrastructure, particularly their markers of cellular stress such as mitochondrion elongation and dystrophy, ER and Golgi apparatus cisternae dilation, and extracellular digestion, were mainly affected by sex chromosomes. The stress response

is known to be largely driven by glucocorticoids, which, as sex hormones, are derived from cholesterol [125]. Receptor availability and sensitivity to glucocorticoids exhibit notable sex differences. Female adult rats (around 10 weeks of age) tend to have increased glucocorticoid receptor expression in infralimbic excitatory neurons, making them more susceptible to reactivity under chronic stress. In contrast, male rats are more responsive to acute stressors [126, 127]. In the context of cardiovascular diseases – a condition more prevalent in men than in women during reproductive years – females are less susceptible to oxidative stress, with reactive oxygen species (ROS) being produced at higher levels in male vascular cells compared to female ones [128]. Given the brain's high metabolic activity, it generates a substantial amount of ROS [129], which has been linked to the development of numerous neurodegenerative diseases [130–132]. However, specific sex differences in ROS levels within the brain, particularly in sexually dimorphic regions, remain to be fully explored.

Additionally, we observed that our WT mouse microglia exhibited more contacts with pre- and post-synaptic elements in a sex-specific manner. Microglia are known for pruning synapses, particularly during early postnatal development [14, 18, 20, 133]. For example, in the P14 CA1 hippocampal region, synapse density (including both pre- and post-synaptic terminals seen with a transmission electron microscope) was reported to be significantly higher in female mice compared to males [134]. This was associated with increased CD68 expression by microglia, coupled to thick long processes and large cell bodies, and closer microglial proximity to synaptic sites. Furthermore, in Thy1-GFP reporter mice at the same age and in the same region, the research also found that bouton density – bulbous axonal endings where neurotransmitters are released, representing pre-synaptic terminals – was higher in females [134]. Although investigations into microglial interactions with synaptic elements during adulthood and under homeostatic conditions remain limited, our findings suggest that FCG mice may have an overall reduction in contact with synaptic elements compared to WT mice.

We also observed that the ultrastructure of both microglial nuclear and cytoplasmic membranes was influenced by sex chromosomes, particularly in terms of circularity and solidity measured at the nanoscale level. The nanoscale morphological assessment provides much greater sensitivity than conventional confocal microscopy, making it a crucial and complementary approach to unravel these morphological changes [73, 91, 135].

To conclude, the investigation of microglial sex differences under normal physiological conditions is still in its early stages, however, our qualitative analyses highlight some key aspects of the impact of sex chromosomes and sex hormones on various microglial properties at steady-state. Although further investigation is required in response to various challenges from the lifestyle and environment (e.g., stress, diet, infection), these properties can have significant implications for health. Generally, denser microglia are associated with increased surveillance of the parenchyma, during which microglia exert physiological roles important for synaptic plasticity, learning and memory [79]. Additionally, longer and more ramified branches are typically linked to increased microglial surveillance and the release of neurotrophic factors that can notably modulate synaptic plasticity [82, 124]. Ramified microglia with ball-and-chain structures are further involved in phagocytosis during normal physiological conditions, notably in the context of adult hippocampal neurogenesis [136]. Microglial organelles such as mitochondria and the ER/Golgi are also expected to maintain healthy functionality, with minimal lysosomal material accumulation, keeping these cells in an active state involved in surveillance and brain remodeling [28, 77].

Conclusion and perspectives

In conclusion, multiple microglial features, including density and distribution, morphology and, ultrastructure were differently shaped by both sex hormones and sex chromosomes in the ventral hippocampus of adult FCG and WT mice during normal physiological conditions. Microglial density, distribution and morphology are mostly affected by the complex interaction of sex chromosomes and hormones in the CA1 Rad and CA1 LMol as well as in the PoDG. Additionally, we show that peripheral myeloid cell infiltration is predominantly increased in the FCG XX in the CA1 LMol. On the other hand, microglial ultrastructure relies mostly on chromosomal influences. Signs of cellular stress, such as mitochondrion elongation and dystrophy as well as ER/Golgi cisternae dilation were mostly chromosomally driven. These findings emphasize the complex interplay between sex hormones and chromosomes in modulating brain immunity.

Studying sex differences is crucial, particularly as this topic has been historically overlooked. The regulation of microglial properties is highly dependent on various factors such as brain region, disease, age, species, and sex, all of which contribute to driving diverse functional outcomes and can have significant clinical implications. The sex-dependent differences in microglia at steady-state can impact the susceptibility to a wide variety of neurodevelopmental, neuropsychiatric and neurodegenerative disorders across life, and the sex chromosomal by sex hormonal investigation under physiological conditions could aid in providing more targeted therapeutical strategies that consider the patient sex. Moreover, the use of

genetic models, such as the FCG, reveals additional layers of complexity, as we pointed out some discrepancies in microglial properties between FCG and WT mice. Accounting for variables such as genetic background, hormonal status and estrous cycle in future investigations would allow for more accurate conclusions, reducing variability and improving reproducibility across studies. Thus, the study of sex differences can lead to a more comprehensive understanding of brain immunity and potentially lead to more specific therapies for multiple diseases that show sex prevalences and in which microglia are implicated throughout the lifespan.

Abbreviations

ATP	Adenosine triphosphate
BBB	Blood-brain barrier
BV	Blood vessel
CA	Cornu ammonis
Cx3Cr1	C-X3-C Motif Chemokine Receptor 1
DCX	Doublecortin
DEGs	Differently expressed genes
DG	Dentate gyrus
eGFP	Enhanced green fluorescent protein
ERα andβ	Estrogen receptors alpha and beta
FACS	Fluorescence-activated cell sorting
GABA	Gamma-aminobutyric acid
Iba1	Ionized calcium binding adapter protein 1
IFNγ	Interferon gamma
IL-1β	Interleukin 1 beta
Ki-67	Ki-67 antigen
NuTRAP	Nuclear tagging and translating ribosome affinity purification
OVX	Ovariectomy
PAMPs	Pathogen-associated molecular patterns
POA	Preoptic area
RNA	Ribonucleic acid
ROS	Reactive oxygen species
Sry	Sex determining region Y
TMEM119	Transmembrane protein 119
TNFα	Tumor necrosis factor alpha
TLRs	Toll-like receptors
WT	Wild-type

Supplementary Information

The online version contains supplementary material available at https://doi.org/10.1186/s12974-025-03341-6.

Supplementary Material 1

Supplementary Material 2

Supplementary Material 3

Supplementary Material 4

Acknowledgements

We acknowledge with respect the Lekwungen-speaking peoples on whose traditional territory the university stands and the Songhees, Esquimalt and WSÁNEĆ peoples whose historical relationships with the land continue to this day. We thank Dr. Katherine Picard and Dr. Haley Vecchiarelli for their insightful discussions and overall training, and Capri Eyres and Dr. Elizabeth Toyin Akinluyi who helped acquire confocal pictures. We are lastly most grateful to the CAMTEC Facility at the University of Victoria for confocal imaging.

Author contributions

BCB: Led project conceptualization, mouse brain intracardiac perfusions, conducted the experiments, imaging and analyses, as well as manuscript writing, figures creation and reviewing. MK: Performed mouse brain intracardiac perfusions, prepared samples for electron microscopy (EM), conducted the EM imaging, performed the EM cytoplasmic and nuclear measurements and provided revisions. OB: Aided the project conceptualization and imaging, helped to perform microglial density analysis and provided revisions. EGA: Helped with the EM analysis and provided revisions. MG: Helped with confocal imaging and provided revisions. MA: Aided the confocal imaging and statistical analyses, as well as provided revisions. MC: Provided overall training and revisions. JB and MR: Prepared, perfused and provided the FCG mouse tissue in addition to reviewing the final draft. M-ÈT: Funding acquisition, resources, overall project supervision, and reviewing of the manuscript.

Funding

BCB and EGA were supported by master's scholarships from the Faculty of Graduate Studies and the Division of Medical Sciences at the University of Victoria. MG received an undergraduate research award from the Natural Sciences and Engineering Research Council of Canada (NSERC). MC was supported by a doctoral training award from the Fonds de Recherche du Québec–Santé (FRQS). MR was supported by a Project Grant from the Canadian Institutes of Health Research (CIHR; #PJT191944) and is a Senior Scholar of the FRQS. The Tremblay Lab's Zeiss Crossbeam 350 scanning electron microscope was acquired with funding from a Canada Foundation for Innovation John R. Evans Leaders Fund grant (#39965 Laboratory of ultrastructural insights into the neurobiology of aging and cognition). This work was supported by a project grant from the CIHR (#PJT461831) awarded to M-ÈT and a Canada Research Chair (Tier II) in ***Neurobiology of Aging and Cognition***. This research was also funded by an NSERC Discovery grant (RGPIN-2024-06043) awarded to M-ÈT.

Data availability

All data generated or analysed during this study are included in this published article and its supplementary information files. The datasets used and/or analysed during the current study are available from the corresponding author on reasonable request.

Declarations

Ethics approval

All animal experiments and procedures were approved by the Université Laval (2021-830 and 2023-1372) and the University of Victoria (AUP 2020-013) animal care committees, strictly following the recommendations from the Canadian Council on Animal Care.

Consent for publication

Not applicable.

Competing interests

The authors declare no competing interests.

Author details

[1]Division of Medical Sciences, University of Victoria, Victoria, BC, Canada
[2]Centre for Advanced Materials and Related Technology (CAMTEC), University of Victoria, Victoria, BC, Canada
[3]Axe neurosciences, Centre de recherche du CHU de Québec-Université Laval, Québec City, QC, Canada
[4]Département de psychiatrie et de neurosciences, Faculté de médecine, Université Laval, Québec City, QC, Canada
[5]Département de médecine moléculaire, Faculté de médecine, Université Laval, Québec City, QC, Canada
[6]Department of Biochemistry and Molecular Biology, The University of British Columbia, Vancouver, BC, Canada
[7]Department of Neurology and Neurosurgery, McGill University, Montréal, QC, Canada
[8]Institute on Aging and Lifelong Health (IALH), University of Victoria, Victoria, BC, Canada

Received: 16 October 2024 / Accepted: 9 January 2025
Published online: 24 January 2025

References

1. DeCasien AR, Guma E, Liu S, Raznahan A. Sex differences in the human brain: a roadmap for more careful analysis and interpretation of a biological reality. Biology Sex Differences. 2022;13:43.
2. Nojima T, Rings A, Allen AM, Otto N, Verschut TA, Billeter J-C, et al. A sex-specific switch between visual and olfactory inputs underlies adaptive sex differences in behavior. Curr Biol. 2021;31:1175–e11916.
3. Alfano V, Cavaliere C, Di Cecca A, Ciccarelli G, Salvatore M, Aiello M, et al. Sex differences in functional brain networks involved in interoception: an fMRI study. Front Neurosci. 2023;17:1130025.
4. Ratnu VS, Emami MR, Bredy TW. Genetic and epigenetic factors underlying sex differences in the regulation of gene expression in the brain. J Neurosci Res. 2017;95:301–10.
5. Weber CM, Clyne AM. Sex differences in the blood–brain barrier and neurodegenerative diseases. APL Bioeng. 2021;5:011509.
6. Westergaard D, Moseley P, Sørup FKH, Baldi P, Brunak S. Population-wide analysis of differences in disease progression patterns in men and women. Nat Commun. 2019;10:666.
7. Park J-C, Lim H, Byun MS, Yi D, Byeon G, Jung G, et al. Sex differences in the progression of glucose metabolism dysfunction in Alzheimer's disease. Exp Mol Med. 2023;55:1023–32.
8. Harley R, Goodfellow VN. The biochemical role of SRY in sex determination. Mol Reprod Dev. 1994;39:184–93.
9. Corre C, Friedel M, Vousden DA, Metcalf A, Spring S, Qiu LR, et al. Separate effects of sex hormones and sex chromosomes on brain structure and function revealed by high-resolution magnetic resonance imaging and spatial navigation assessment of the four core genotype mouse model. Brain Struct Funct. 2016;221:997–1016.
10. Bobotis BC, Braniff O, Gargus M, Akinluyi ET, Awogbindin IO, Tremblay M-È. Sex differences of microglia in the healthy brain from embryonic development to adulthood and across lifestyle influences. Brain Res Bull. 2023;202:110752.
11. Bramble MS, Lipson A, Vashist N, Vilain E. Effects of chromosomal sex and hormonal influences on shaping sex differences in brain and behavior: lessons from cases of disorders of sex development. J Neurosci Res. 2017;95:65–74.
12. Hiort O. The differential role of androgens in early human sex development. BMC Med. 2013;11:152.
13. Spritzer MD, Galea LAM. Testosterone and dihydrotestosterone, but not estradiol, enhance survival of new hippocampal neurons in adult male rats. Dev Neurobiol. 2007;67:1321–33.
14. Hui CW, Vecchiarelli HA, Gervais É, Luo X, Michaud F, Scheefhals L, et al. Sex differences of Microglia and synapses in the hippocampal dentate gyrus of adult mouse offspring exposed to maternal Immune activation. Front Cell Neurosci. 2020;14:558181.
15. Loiola RA, Wickstead ES, Solito E, McArthur S. Estrogen promotes pro-resolving microglial behavior and phagocytic cell clearance through the actions of annexin A1. Front Endocrinol (Lausanne). 2019;10:420.
16. Bordeleau M, Lacabanne C, Fernández de Cossío L, Vernoux N, Savage JC, González-Ibáñez F, et al. Microglial and peripheral immune priming is partially sexually dimorphic in adolescent mouse offspring exposed to maternal high-fat diet. J Neuroinflamm. 2020;17:264.
17. Schwarz JM, Sholar PW, Bilbo SD. Sex differences in microglial colonization of the developing rat brain. J Neurochem. 2012;120:948–63.
18. Lenz KM, Nugent BM, Haliyur R, McCarthy MM. Microglia are essential to masculinization of Brain and Behavior. J Neurosci. 2013;33:2761–72.
19. Doyle HH, Eidson LN, Sinkiewicz DM, Murphy AZ. Sex differences in Microglia Activity within the Periaqueductal Gray of the rat: a potential mechanism driving the Dimorphic effects of Morphine. J Neurosci. 2017;37:3202–14.
20. Weinhard L, Neniskyte U, Vadisiute A, di Bartolomei G, Aygün N, Riviere L, et al. Sexual dimorphism of microglia and synapses during mouse postnatal development. Dev Neurobiol. 2018;78:618–26.
21. Tremblay M-È. Microglial functional alteration and increased diversity in the challenged brain: insights into novel targets for intervention. Brain Behav Immun - Health. 2021;16:100301.
22. Tremblay M-È, Majewska AK. Ultrastructural Analyses of Microglial Interactions with synapses. Methods Mol Biol. 2019;2034:83–95.
23. Venturino A, Schulz R, De Jesús-Cortés H, Maes ME, Nagy B, Reilly-Andújar F, et al. Microglia enable mature perineuronal nets disassembly upon anesthetic ketamine exposure or 60-Hz light entrainment in the healthy brain. Cell Rep. 2021;36:109313.
24. Nguyen PT, Dorman LC, Pan S, Vainchtein ID, Han RT, Nakao-Inoue H, et al. Microglial remodeling of the Extracellular Matrix promotes synapse plasticity. Cell. 2020;182:388–e40315.
25. Filipello F, Morini R, Corradini I, Zerbi V, Canzi A, Michalski B, et al. The Microglial Innate Immune receptor TREM2 is required for synapse elimination and normal brain connectivity. Immunity. 2018;48:979–e9918.
26. Jiang T, Zhang Y-D, Gao Q, Zhou J-S, Zhu X-C, Lu H, et al. TREM1 facilitates microglial phagocytosis of amyloid beta. Acta Neuropathol. 2016;132:667–83.
27. St-Pierre M-K, Bordeleau M, Tremblay M-È. Visualizing dark microglia. Methods Mol Biol. 2019;2034:97–110. https://doi.org/10.1007/978-1-4939-9658-2_8.
28. St-Pierre M-K, Carrier M, Lau V, Tremblay M-È. Investigating microglial ultrastructural alterations and intimate relationships with neuronal stress, dystrophy, and degeneration in mouse models of Alzheimer's Disease. Methods Mol Biol. 2022;2515:29–58.
29. Juraska JM, Sisk CL, DonCarlos LL. Sexual differentiation of the adolescent rodent brain: hormonal influences and developmental mechanisms. Horm Behav. 2013;64:203–10.
30. Alliot F, Godin I, Pessac B. Microglia derive from progenitors, originating from the yolk sac, and which proliferate in the brain. Brain Res Dev Brain Res. 1999;117:145–52.
31. Welsh M, Saunders PTK, Fisken M, Scott HM, Hutchison GR, Smith LB, et al. Identification in rats of a programming window for reproductive tract masculinization, disruption of which leads to hypospadias and cryptorchidism. J Clin Invest. 2008;118:1479–90.
32. Habert R, Picon R. Testosterone, dihydrotestosterone and estradiol-17 beta levels in maternal and fetal plasma and in fetal testes in the rat. J Steroid Biochem. 1984;21:193–8.
33. Keller D, Erö C, Markram H. Cell densities in the mouse brain: a systematic review. Front Neuroanat. 2018;12:83.
34. Sauer J-F, Bartos M. The role of the dentate gyrus in mnemonic functions. Neuroforum. 2020;26:247–54.
35. García-Ovejero D, Veiga S, García-Segura LM, Doncarlos LL. Glial expression of estrogen and androgen receptors after rat brain injury. J Comp Neurol. 2002;450:256–71.
36. Habib P, Dreymueller D, Ludwig A, Beyer C, Dang J. Sex steroid hormone-mediated functional regulation of microglia-like BV-2 cells during hypoxia. J Steroid Biochem Mol Biol. 2013;138:195–205.
37. Wu W, Tan X, Dai Y, Krishnan V, Warner M, Gustafsson J-Å. Targeting estrogen receptor β in microglia and T cells to treat experimental autoimmune encephalomyelitis. Proc Natl Acad Sci. 2013;110:3543–8.
38. Bisht K, Sharma KP, Lecours C, Sánchez MG, El Hajj H, Milior G, et al. Dark microglia: a new phenotype predominantly associated with pathological states. Glia. 2016;64:826–39.
39. Anderson AG, Rogers BB, Loupe JM, Rodriguez-Nunez I, Roberts SC, White LM, et al. Single nucleus multiomics identifies ZEB1 and MAFB as candidate regulators of Alzheimer's disease-specific cis-regulatory elements. Cell Genomics. 2023;3:100263.
40. Lavisse S, Goutal S, Wimberley C, Tonietto M, Bottlaender M, Gervais P, et al. Increased microglial activation in patients with Parkinson disease using [18F]-DPA714 TSPO PET imaging. Parkinsonism Relat Disord. 2021;82:29–36.
41. Bovenzi R, Sancesario GM, Conti M, Grillo P, Cerroni R, Bissacco J, et al. Sex hormones differentially contribute to Parkinson disease in males: a multimodal biomarker study. Eur J Neurol. 2023;30:1983–90.
42. Lopez-Lee C, Torres ERS, Carling G, Gan L. Mechanisms of sex differences in Alzheimer's disease. Neuron. 2024;112:1208–21.
43. Doss PMIA, Umair M, Baillargeon J, Fazazi R, Fudge N, Akbar I, et al. Male sex chromosomal complement exacerbates the pathogenicity of Th17 cells in a chronic model of central nervous system autoimmunity. Cell Rep. 2021;34:108833.
44. Guneykaya D, Ivanov A, Hernandez DP, Haage V, Wojtas B, Meyer N, et al. Transcriptional and Translational Differences of Microglia from male and female brains. Cell Rep. 2018;24:2773–e27836.
45. Villa A, Gelosa P, Castiglioni L, Cimino M, Rizzi N, Pepe G, et al. Sex-specific features of Microglia from Adult mice. Cell Rep. 2018;23:3501–11.
46. Gildawie KR, Orso R, Peterzell S, Thompson V, Brenhouse HC. Sex differences in prefrontal cortex microglia morphology: impact of a two-hit model of adversity throughout development. Neurosci Lett. 2020;738:135381.
47. Itoh Y, Mackie R, Kampf K, Domadia S, Brown JD, O'Neill R, et al. Four core genotypes mouse model: localization of the sry transgene and bioassay for testicular hormone levels. BMC Res Notes. 2015;8:69.

48. Lovell-Badge R, Robertson E. XY female mice resulting from a heritable mutation in the primary testis determining gene, Tdy. Development. 1990;109:635–46.
49. De Vries GJ, Rissman EF, Simerly RB, Yang L-Y, Scordalakes EM, Auger CJ, et al. A model system for study of sex chromosome effects on sexually dimorphic neural and behavioral traits. J Neurosci. 2002;22:9005–14.
50. Bordeleau M, Carrier M, Luheshi GN, Tremblay M-È. Microglia along sex lines: from brain colonization, maturation and function, to implication in neurodevelopmental disorders. Semin Cell Dev Biol. 2019;94:152–63.
51. Hojo Y, Higo S, Kawato S, Hatanaka Y, Ooishi Y, Murakami G, et al. Hippocampal synthesis of sex steroids and corticosteroids: essential for modulation of synaptic plasticity. Front Endocrinol (Lausanne). 2011;2:43. https://www.ncbi.nlm.nih.gov/pmc/articles/PMC3356120/
52. Hojo Y, Murakami G, Mukai H, Higo S, Hatanaka Y, Ogiue-Ikeda M, et al. Estrogen synthesis in the brain—role in synaptic plasticity and memory. Mol Cell Endocrinol. 2008;290:31–43.
53. Ooishi Y, Kawato S, Hojo Y, Hatanaka Y, Higo S, Murakami G, et al. Modulation of synaptic plasticity in the hippocampus by hippocampus-derived estrogen and androgen. J Steroid Biochem Mol Biol. 2012;131:37–51.
54. Fanselow MS, Dong H-W. Are the dorsal and ventral Hippocampus functionally distinct structures? Neuron. 2010;65:7–19.
55. Jinno S, Klausberger T, Marton LF, Dalezios Y, Roberts JDB, Fuentealba P, et al. Neuronal diversity in GABAergic Long-Range projections from the Hippocampus. J Neurosci. 2007;27:8790–804.
56. De Felice E, Gonçalves de Andrade E, Golia MT, González Ibáñez F, Khakpour M, Di Castro MA, et al. Microglial diversity along the hippocampal longitudinal axis impacts synaptic plasticity in adult male mice under homeostatic conditions. J Neuroinflamm. 2022;19:292.
57. González Ibáñez F, Halvorson T, Sharma K, McKee CG, Carrier M, Picard K, et al. Ketogenic diet changes microglial morphology and the hippocampal lipidomic profile differently in stress susceptible versus resistant male mice upon repeated social defeat. Brain Behav Immun. 2023;114:383–406.
58. Khakpour M, Ibáñez FG, Bordeleau M, Picard K, Mckee-Reid L, Ben-Azu B, et al. Manual versus automatic analysis of microglial density and distribution: a comparison in the hippocampus of healthy and lipopolysaccharide-challenged mature male mice. Micron. 2022;161:103334.
59. Sharon A, Erez H, Spira ME. Significant sex differences in the efficacy of the CSF1R Inhibitor-PLX5622 on rat brain Microglia Elimination. Pharmaceuticals. 2022;15:569.
60. Bender RA, Zhou L, Vierk R, Brandt N, Keller A, Gee CE, et al. Sex-dependent regulation of aromatase-mediated synaptic plasticity in the Basolateral Amygdala. J Neurosci. 2017;37:1532–45.
61. Bakker J, Baum MJ. Role for estradiol in female-typical brain and behavioral sexual differentiation. Front Neuroendocrinol. 2008;29:1–16.
62. Vousden DA, Corre C, Spring S, Qiu LR, Metcalf A, Cox E, et al. Impact of X/Y genes and sex hormones on mouse neuroanatomy. NeuroImage. 2018;173:551–63.
63. Arnold AP. X chromosome agents of sexual differentiation. Nat Rev Endocrinol. 2022;18:574–83.
64. González Ibanez F, Picard K, Bordeleau M, Sharma K, Bisht K, Tremblay M-È. Immunofluorescence staining using IBA1 and TMEM119 for microglial density, morphology and peripheral myeloid cell infiltration analysis in mouse brain. J Vis Exp. 2019.
65. Bobotis BC, Halvorson T, Carrier M, Tremblay M-È. Established and emerging techniques for the study of microglia: visualization, depletion, and fate mapping. Front Cell Neurosci. 2024;18:1317125.
66. Carrier M, Robert M-È, St-Pierre M-K, Ibáñez FG, Gonçalves de Andrade E, Laroche A, et al. Bone marrow-derived myeloid cells transiently colonize the brain during postnatal development and interact with glutamatergic synapses. iScience. 2024;27:110037.
67. Vankriekelsvenne E, Chrzanowski U, Manzhula K, Greiner T, Wree A, Hawlitschka A, et al. Transmembrane protein 119 is neither a specific nor a reliable marker for microglia. Glia. 2022;70:1170–90.
68. Franklin KBJ, Paxinos G. Paxinos and Franklin's The mouse brain in stereotaxic coordinates. Fourth edition. Amsterdam: Academic Press, an imprint of Elsevier; 2013.
69. Picard K, Corsi G, Decoeur F, Di Castro MA, Bordeleau M, Persillet M, et al. Microglial homeostasis disruption modulates non-rapid eye movement sleep duration and neuronal activity in adult female mice. Brain Behav Immun. 2023;107:153–64.
70. Leyh J, Paeschke S, Mages B, Michalski D, Nowicki M, Bechmann I, et al. Classification of microglial morphological phenotypes using machine learning. Front Cell Neurosci. 2021;15:701673.
71. Bankhead P, Loughrey MB, Fernández JA, Dombrowski Y, McArt DG, Dunne PD, et al. QuPath: open source software for digital pathology image analysis. Sci Rep. 2017;7:16878.
72. Savage JC, Picard K, González-Ibáñez F, Tremblay M-È. A brief history of microglial ultrastructure: distinctive features, phenotypes, and functions discovered over the past 60 years by electron microscopy. Front Immunol. 2018;9:803.
73. Nahirney PC, Tremblay M-E. Brain ultrastructure: putting the Pieces together. Front Cell Dev Biol. 2021;9:629503.
74. Steinfeld N, Ma C-IJ, Maxfield FR. Signaling pathways regulating the extracellular digestion of lipoprotein aggregates by macrophages. Mol Biol Cell. 2024;35:ar5.
75. Digestive exophagy. Phagocyte digestion of objects too large for phagocytosis - Maxfield – 2020 - Traffic - Wiley Online Library [Internet]. [cited 2024 Dec 5]. Available from: https://onlinelibrary.wiley.com/doi/https://doi.org/10.1111/tra.12712
76. Bordeleau M, Fernández de Cossío L, Lacabanne C, Savage JC, Vernoux N, Chakravarty M, et al. Maternal high-fat diet modifies myelin organization, microglial interactions, and results in social memory and sensorimotor gating deficits in adolescent mouse offspring. Brain Behav Immun Health. 2021;15:100281.
77. St-Pierre M-K, Carrier M, González Ibáñez F, Šimončičová E, Wallman M-J, Vallières L, et al. Ultrastructural characterization of dark microglia during aging in a mouse model of Alzheimer's disease pathology and in human post-mortem brain samples. J Neuroinflammation. 2022;19:235.
78. Iovino L, VanderZwaag J, Kaur G, Khakpour M, Giusti V, Donadon M, et al. Investigation of microglial diversity in a LRRK2 G2019S mouse model of Parkinson's disease. Neurobiol Dis. 2024;195:106481.
79. Rodríguez JJ, Witton J, Olabarria M, Noristani HN, Verkhratsky A. Increase in the density of resting microglia precedes neuritic plaque formation and microglial activation in a transgenic model of Alzheimer's disease. Cell Death Dis. 2010;1:e1–1.
80. Ju H, Park KW, Kim I, Cave JW, Cho S. Phagocytosis converts infiltrated monocytes to microglia-like phenotype in experimental brain ischemia. J Neuroinflamm. 2022;19:190.
81. Vidal-Itriago A, Radford RAW, Aramideh JA, Maurel C, Scherer NM, Don EK, et al. Microglia morphophysiological diversity and its implications for the CNS. Front Immunol. 2022;13:997786.
82. Savage JC, Carrier M, Tremblay M-È. Morphology of Microglia Across Contexts of Health and Disease. Methods Mol Biol. 2019;2034:13–26.
83. Paolicelli RC, Sierra A, Stevens B, Tremblay M-E, Aguzzi A, Ajami B, et al. Microglia states and nomenclature: a field at its crossroads. Neuron. 2022;110:3458–83.
84. Colombo G, Cubero RJA, Kanari L, Venturino A, Schulz R, Scolamiero M, et al. A tool for mapping microglial morphology, morphOMICs, reveals brain-region and sex-dependent phenotypes. Nat Neurosci. 2022;25:1379–93.
85. Zanier ER, Fumagalli S, Perego C, Pischiutta F, De Simoni M-G. Shape descriptors of the never resting microglia in three different acute brain injury models in mice. Intensive Care Med Experimental. 2015;3:7.
86. Maras PM, Hebda-Bauer EK, Hagenauer MH, Hilde KL, Blandino P, Watson SJ, et al. Differences in microglia morphological profiles reflect divergent emotional temperaments: insights from a selective breeding model. Transl Psychiatry. 2022;12:1–11.
87. Šišková Z, Tremblay M-È. Microglia and synapse: interactions in health and neurodegeneration. Neural Plast. 2013;2013:425845.
88. Fujikawa R, Jinno S. Identification of hyper-ramified microglia in the CA1 region of the mouse hippocampus potentially associated with stress resilience. Eur J Neurosci. 2022;56:5137–53.
89. Streit WJ, Braak H, Xue Q-S, Bechmann I. Dystrophic (senescent) rather than activated microglial cells are associated with tau pathology and likely precede neurodegeneration in Alzheimer's disease. Acta Neuropathol. 2009;118:475–85.
90. Bisht K, Sharma KP, Lecours C, Gabriela Sánchez M, El Hajj H, Milior G, et al. Dark microglia: a new phenotype predominantly associated with pathological states. Glia. 2016;64:826–39.
91. El Hajj H, Savage JC, Bisht K, Parent M, Vallières L, Rivest S, et al. Ultrastructural evidence of microglial heterogeneity in Alzheimer's disease amyloid pathology. J Neuroinflammation. 2019;16:87.

92. She Z-Y, Yang W-X. Sry and SoxE genes: how they participate in mammalian sex determination and gonadal development? Semin Cell Dev Biol. 2017;63:13–22.
93. Kenchappa RS, Diwakar L, Annepu J, Ravindranath V. Estrogen and neuroprotection: higher constitutive expression of glutaredoxin in female mice offers protection against MPTP-mediated neurodegeneration. FASEB J. 2004;18:1102–4.
94. Tukiainen T, Villani A-C, Yen A, Rivas MA, Marshall JL, Satija R, et al. Landscape of X chromosome inactivation across human tissues. Nature. 2017;550:244–8.
95. Tharp ME, Han CZ, Balak CD, Fitzpatrick C, O'Connor C, Preissl S et al. The inactive X chromosome drives sex differences in microglial inflammatory activity in human glioblastoma. bioRxiv. 2024;2024.06.06.597433.
96. Ocañas SR, Pham KD, Cox JEJ, Keck AW, Ko S, Ampadu FA, et al. Microglial senescence contributes to female-biased neuroinflammation in the aging mouse hippocampus: implications for Alzheimer's disease. J Neuroinflamm. 2023;20:188.
97. Christine Knickmeyer R, Baron-Cohen S. Fetal testosterone and sex differences. Early Hum Dev. 2006;82:755–60.
98. Isgor C, Watson SJ. Estrogen receptor alpha and beta mRNA expressions by proliferating and differentiating cells in the adult rat dentate gyrus and subventricular zone. Neuroscience. 2005;134:847–56.
99. Arnold AP, Chen X. What does the four core genotypes mouse model tell us about sex differences in the brain and other tissues? Front Neuroendocrinol. 2009;30:1–9.
100. Markham JA, Jurgens HA, Auger CJ, De Vries GJ, Arnold AP, Juraska JM. Sex differences in mouse cortical thickness are independent of the complement of sex chromosomes. Neuroscience. 2003;116:71–5.
101. Wagner CK, Xu J, Pfau JL, Quadros PS, De Vries GJ, Arnold AP. Neonatal mice possessing an sry transgene show a masculinized pattern of progesterone receptor expression in the brain independent of sex chromosome status. Endocrinology. 2004;145:1046–9.
102. Acaz-Fonseca E, Duran JC, Carrero P, Garcia-Segura LM, Arevalo MA. Sex differences in glia reactivity after cortical brain injury. Glia. 2015;63:1966–81.
103. De Felice E, Bobotis BC, Rigillo G, Khakpour M, Gonçalves de Andrade E, Benatti C, et al. Female mice exhibit similar long-term plasticity and microglial properties between the dorsal and ventral hippocampal poles. Brain Behav Immun. 2025;124:192–204. https://www.sciencedirect.com/science/article/pii/S0889159124007232
104. Bennett A, Baker C, Alward T, Vanner S, Reed D, Lomax A. The impact of the Estrous Cycle on Abdominal Pain. Physiology. 2024;39:1202.
105. Velez-Perez A, Holder MK, Fountain S, Blaustein JD. Estradiol increases microglial response to lipopolysaccharide in the ventromedial hpothalamus during the peripubertal sensitive period in female mice. eNeuro. 2020;7:ENEURO.0505-19.2020.
106. Ghosh MK, Chen K-HE, Dill-Garlow R, Ma LJ, Yonezawa T, Itoh Y, et al. Sex differences in the immune system become evident in the perinatal period in the four core genotypes mouse. Front Endocrinol (Lausanne). 2021;12:582614.
107. Qi S, Mamun AA, Ngwa C, Romana S, Ritzel R, Arnold AP, et al. X chromosome escapee genes are involved in ischemic sexual dimorphism through epigenetic modification of inflammatory signals. J Neuroinflamm. 2021;18:70.
108. Panten J, Del Prete S, Cleland JP, Saunders LM, van Riet J, Schneider A, et al. Four core genotypes mice harbour a 3.2 MB X-Y translocation that perturbs Tlr7 dosage. Nat Commun. 2024;15:8814.
109. Schilling S, Chausse B, Dikmen HO, Almouhanna F, Hollnagel J-O, Lewen A, et al. TLR2- and TLR3-activated microglia induce different levels of neuronal network dysfunction in a context-dependent manner. Brain Behav Immun. 2021;96:80–91.
110. Michaelis KA, Norgard MA, Levasseur PR, Olson B, Burfeind KG, Buenafe AC, et al. Persistent toll-like receptor 7 stimulation induces behavioral and molecular innate immune tolerance. Brain Behav Immun. 2019;82:338–53.
111. Perkins AE, Piazza MK, Deak T. Stereological analysis of microglia in aged male and female Fischer 344 rats in socially-relevant brain regions. Neuroscience. 2018;377:40–52.
112. Cooke PS, Nanjappa MK, Ko C, Prins GS, Hess RA. Estrogens in male physiology. Physiol Rev. 2017;97:995–1043.
113. Ärnlöv J, Pencina MJ, Amin S, Nam B-H, Benjamin EJ, Murabito JM, et al. Endogenous sex hormones and Cardiovascular Disease incidence in men. Ann Intern Med. 2006;145:176–84.
114. Khalil RA, Estrogen. Vascular estrogen receptor and hormone therapy in Postmenopausal Vascular Disease. Biochem Pharmacol. 2013;86. https://doi.org/10.1016/j.bcp.2013.09.024.
115. Maggioli E, McArthur S, Mauro C, Kieswich J, Kusters DHM, Reutelingsperger CPM, et al. Estrogen protects the blood-brain barrier from inflammation-induced disruption and increased lymphocyte trafficking. Brain Behav Immun. 2016;51:212–22.
116. Bake S, Sohrabji F. 17β-Estradiol differentially regulates blood-brain barrier permeability in Young and Aging Female rats. Endocrinology. 2004;145:5471–5.
117. Bohnert S, Seiffert A, Trella S, Bohnert M, Distel L, Ondruschka B, et al. TMEM119 as a specific marker of microglia reaction in traumatic brain injury in postmortem examination. Int J Legal Med. 2020;134:2167–76.
118. Kaiser T, Feng G. Tmem119-EGFP and Tmem119-CreERT2 Transgenic Mice for Labeling and Manipulating Microglia. eNeuro. 2019;6:ENEURO.0448-18.2019.
119. Ma W, Oswald J, Rios Angulo A, Chen Q. Tmem119 expression is downregulated in a subset of brain metastasis-associated microglia. BMC Neurosci. 2024;25:6.
120. Ruan C, Elyaman W. A New understanding of TMEM119 as a marker of Microglia. Front Cell Neurosci. 2022;16:902372.
121. Kenkhuis B, Somarakis A, Kleindouwel LRT, van Roon-Mom WMC, Höllt T, van der Weerd L. Co-expression patterns of microglia markers Iba1, TMEM119 and P2RY12 in Alzheimer's disease. Neurobiol Dis. 2022;167:105684.
122. Young K, Rothers J, Castaneda S, Ritchie J, Pottenger AE, Morrison HW. Sex and regional differences in microglia morphology and complement receptor 3 are independent of constitutive neuroinflammatory protein concentrations in healthy mice [Internet]. PeerJ Inc.; 2018 May. Report No.: e26937v1. Available from: https://peerj.com/preprints/26937
123. Mitran SI, Burada E, Tănasie CA, Manea NC, Ciorbagiu MC, Mirea CS, et al. Microglial morphology determined with confocal and two-photon laser scanning microscopy. Rom J Morphol Embryol. 2018;59:485–90.
124. Davies DS, Ma J, Jegathees T, Goldsbury C. Microglia show altered morphology and reduced arborization in human brain during aging and Alzheimer's disease. Brain Pathol. 2017;27:795–808.
125. Moisan M-P. Sexual dimorphism in glucocorticoid stress response. Int J Mol Sci. 2021;22:3139.
126. Moench KM, Breach MR, Wellman CL. Chronic stress produces enduring sex- and region-specific alterations in novel stress-induced c-Fos expression. Neurobiol Stress. 2019;10:100147.
127. Herman J, Parikh R, Herman JP. Sex and stress: Corticocolimbic Glucocorticoid Signaling Dynamics. Psychoneuroendocrinology. 2024;160:106739.
128. Matarrese P, Colasanti T, Ascione B, Margutti P, Franconi F, Alessandri C, et al. Gender disparity in susceptibility to oxidative stress and apoptosis induced by autoantibodies specific to RLIP76 in vascular cells. Antioxid Redox Signal. 2011;15:2825–36.
129. Massaad CA, Klann E. Reactive oxygen species in the regulation of synaptic plasticity and memory. Antioxid Redox Signal. 2011;14:2013–54.
130. Dash UC, Bhol NK, Swain SK, Samal RR, Nayak PK, Raina V et al. Oxidative stress and inflammation in the pathogenesis of neurological disorders: Mechanisms and implications. Acta Pharmaceutica Sinica B [Internet]. 2024 [cited 2024 Dec 13]; Available from: https://www.sciencedirect.com/science/article/pii/S2211383524004040
131. Esteras N, Kopach O, Maiolino M, Lariccia V, Amoroso S, Qamar S, et al. Mitochondrial ROS control neuronal excitability and cell fate in frontotemporal dementia. Alzheimer's Dement. 2022;18:318–38.
132. Houldsworth A. Role of oxidative stress in neurodegenerative disorders: a review of reactive oxygen species and prevention by antioxidants. Brain Commun. 2024;6:fcad356.
133. Paolicelli RC, Bolasco G, Pagani F, Maggi L, Scianni M, Panzanelli P, et al. Synaptic pruning by microglia is necessary for normal brain development. Science. 2011;333:1456–8.
134. Prengel TM, Brunne B, Habiballa M, Rune GM. Sexually differentiated microglia and CA1 hippocampal synaptic connectivity. J Neuroendocrinol. 2023;35:e13276.
135. Bernier L-P, Bohlen CJ, York EM, Choi HB, Kamyabi A, Dissing-Olesen L, et al. Nanoscale Surveillance of the brain by Microglia via cAMP-Regulated Filopodia. Cell Rep. 2019;27:2895–e29084.
136. Sierra A, Encinas JM, Deudero JJ, Chancey JH, Enikolopov G, Overstreet-Wadiche LS, et al. Microglia shape adult hippocampal neurogenesis through apoptosis-coupled phagocytosis. Cell Stem Cell. 2010;7:483–95.

Publisher's note